

## Mean-Field Approximations With Adaptive Coupling for Networks With Spike-Timing-Dependent Plasticity

**Benoit Duchet**

*benoit.duchet@ndcn.ox.ac.uk*

*Nuffield Department of Clinical Neuroscience, University of Oxford, Oxford X3 9DU, U.K., and MRC Brain Network Dynamics Unit, University of Oxford, Oxford X1 3TH, U.K.*

**Christian Bick**

*c.bick@vu.nl*

*Department of Mathematics, Vrije Universiteit Amsterdam, Amsterdam 1081 HV, the Netherlands; Amsterdam Neuroscience—Systems and Network Neuroscience, Amsterdam 1081 HV, the Netherlands; and Mathematical Institute, University of Oxford, Oxford X2 6GG, U.K.*

**Áine Byrne**

*aine.byrne@ucd.ie*

*School of Mathematics and Statistics, University College Dublin, Dublin D04 V1W8, Ireland*

Understanding the effect of spike-timing-dependent plasticity (STDP) is key to elucidating how neural networks change over long timescales and to design interventions aimed at modulating such networks in neurological disorders. However, progress is restricted by the significant computational cost associated with simulating neural network models with STDP and by the lack of low-dimensional description that could provide analytical insights. Phase-difference-dependent plasticity (PDDP) rules approximate STDP in phase oscillator networks, which prescribe synaptic changes based on phase differences of neuron pairs rather than differences in spike timing. Here we construct mean-field approximations for phase oscillator networks with STDP to describe part of the phase space for this very high-dimensional system. We first show that single-harmonic PDDP rules can approximate a simple form of symmetric STDP, while multiharmonic rules are required to accurately approximate causal STDP. We then derive exact expressions for the evolution of the average PDDP coupling weight in terms of network synchrony. For adaptive networks of Kuramoto oscillators that form clusters, we formulate a family of low-dimensional descriptions based on the mean-field dynamics of each cluster and average coupling weights between and within clusters. Finally, we show that such a two-cluster mean-field model can be

**fitted to synthetic data to provide a low-dimensional approximation of a full adaptive network with symmetric STDP. Our framework represents a step toward a low-dimensional description of adaptive networks with STDP, and could for example inform the development of new therapies aimed at maximizing the long-lasting effects of brain stimulation.**

## 1 Introduction

Synaptic plasticity is considered the primary mechanism for learning and memory consolidation. Neurons with similar activity patterns strengthen their synaptic connections, while others connections may weaken. Spike-timing-dependent plasticity (STDP) has been suggested as an unsupervised, local learning rule in neural networks (Gerstner et al., 1996; Song et al., 2000) motivated by experimental findings (Markram et al., 1997; Bi & Poo, 1998; Feldman, 2000; Froemke & Dan, 2002; Cassenaer & Laurent, 2007; Sgritta et al., 2017). These experimental studies reported synaptic strengthening or weakening depending on the order and timing of pre- and postsynaptic spikes. In causal STDP (see Figure 1A), long-term potentiation (LTP) occurs when the postsynaptic neuron fires shortly after the presynaptic neuron. Conversely, long-term depression (LTD) occurs when the postsynaptic neuron fires shortly before the presynaptic neuron. The closer the spike times are, the larger the effect. Noncausal, symmetric STDP has also been reported in the hippocampus (Abbott & Nelson, 2000; Mishra et al., 2016; see Figure 1B). Although Donald Hebb emphasized the importance of causality in his theory of adaptive synaptic connections in 1949 (Hebb, 2005), such noncausal rules, which neglect temporal precedence, are sometimes referred to as Hebbian plasticity rules.<sup>1</sup>

As a major contributor to long-term plasticity (timescale of 1 s or longer), STDP is key to long-term neural processes in the healthy brain, such as memory (Litwin-Kumar & Doiron, 2014) and sensory encoding (Coulon et al., 2011), but also to modulate networks affected by neurological disorders (Madadi Asl et al., 2022). In particular, long-term plasticity is critical to the design of effective therapies for neurological disorders based on invasive and noninvasive brain stimulation. Paired associative stimulation using transcranial magnetic stimulation (TMS) has been shown to trigger STDP-like changes (Müller-Dahlhaus et al., 2010; Johnen et al., 2015; Wiratman et al., 2022), and STDP models have been used to design electrical stimulation for stroke rehabilitation (Kim et al., 2021). Coordinated reset deep brain stimulation (DBS) for Parkinson's disease was designed to induce long-term plastic changes outlasting stimulation using STDP models

<sup>1</sup>In this work, we call plasticity rules *causal* when temporal precedence is enforced (as in “classical” STDP rules; Bi & Poo, 1998), and *symmetric* when inverting spike timings and phase differences leads to the same type of adaptation. We stay clear of the ambiguous term *Hebbian* STDP, which is also sometimes used to refer to causal STDP in the experimental literature (Cassenaer & Laurent, 2007; Sgritta et al., 2017).

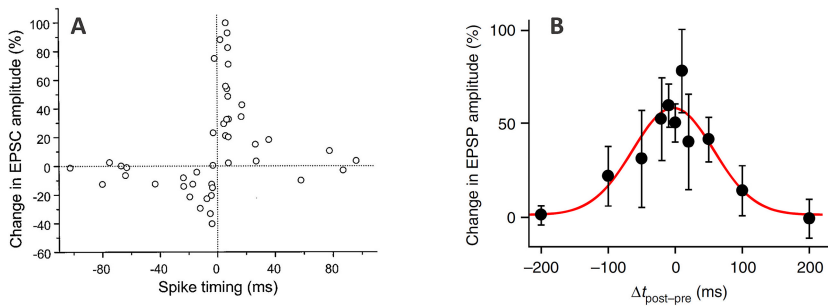


Figure 1: Examples of STDP observed in pairing experiments. In typical STDP pairing experiments, the presynaptic neuron is stimulated shortly before or after forcing the postsynaptic neuron to fire by injecting a brief current pulse (with a controlled delay). The pairing is repeated many times for each value of the delay. (A) Causal STDP in synapses on glutamatergic neurons in rat hippocampal culture. Adapted from Bi and Poo (1998). (B) Symmetric STDP in CA3-CA3 synapses in the hippocampus (slices in the rat). Adapted from Mishra et al. (2016). In both panels, the horizontal axes represent the difference in spike timing (postsynaptic minus presynaptic), and the vertical axes represent measures of the change in synaptic strength, either involving excitatory postsynaptic currents (EPSC, panel A) or excitatory postsynaptic potentials (EPSP, panel B).

(Tass & Majtanik, 2006) and was later validated in nonhuman primates (Tass et al., 2012; Wang et al., 2016) and patients (Adamchic et al., 2014).

However, progress in these areas is restricted by the significant computational cost associated with simulating neural network models with STDP and by the lack of low-dimensional description of such networks. Indeed, simulating networks with STDP of even moderate size for more than a couple of minutes of biological time can be impractical because the number of weight updates scales with the square of the network size. Low-dimensional mean-field approximations have been developed for networks with short-term plasticity (Tsodyks et al., 1998; Taher et al., 2020; Gast et al., 2020; Schmutz et al., 2020; Gast et al., 2021), but reductions for STDP have assumed that plasticity does not change firing rates and spike covariances (Ocker et al., 2015) or that the network is in a balanced state at every point in time (Akil et al., 2021). Even if node dynamics are given by a simple Kuramoto-type model, it is a challenge to understand the dynamics of large networks with adaptivity. While the continuum limit of Kuramoto-type networks with STDP-like adaptivity can be described by integro-differential equations from a theoretical perspective (Gkogkas et al., 2021), these do not necessarily elucidate the resulting network dynamics or yield a computational advantage. Approaches like the Ott-Antonsen reduction (Ott & Antonsen, 2008), which have been instrumental to deriving low-dimensional descriptions of phase oscillators (see Bick et al., 2020) are not directly

applicable to adaptive networks where all connection weights evolve independently of one another. Indeed, one would not expect an exact mean-field description with only a few degrees of freedom to be possible (as for the Kuramoto model with static connectivity) without making further assumptions, as any exact low-dimensional description would have to reflect the high, adaptivity-induced multistability (Berner et al., 2019).

Models of causal, additive STDP based on differences in spike timing are exemplified by the work of Song et al. (2000). They assumed that the synaptic strength  $\kappa_{kl}$  from presynaptic neuron  $l$  to postsynaptic neuron  $k$  is updated only when either neurons spike and the corresponding change in synaptic strength from  $l$  to  $k$  is given by

$$\Delta\kappa_{kl} = \begin{cases} A_+e^{-\Delta t_{kl}/\tau_+} & \text{for } \Delta t_{kl} = t_k - t_l > 0, \\ -A_-e^{-|\Delta t_{kl}|/\tau_-} & \text{for } \Delta t_{kl} < 0, \\ 0 & \text{for } \Delta t_{kl} = 0, \end{cases} \quad (1.1)$$

where the most recent spike times of neurons  $k$  and  $l$  are  $t_k$  and  $t_l$ , the parameters  $A_+$  and  $A_-$  determine the magnitude of LTP and LTD, and  $\tau_+$  and  $\tau_-$  determine the timescale of LTP and LTD, respectively (see Figure 4A). Conversely, symmetric STDP with both LTP and LTD can be modeled by asserting that synaptic strengths are updated when either neuron spikes, with a change in synaptic strength from  $l$  to  $k$  given by the Mexican hat function (Ricker wavelet),

$$\Delta\kappa_{kl} = \frac{2a}{\sqrt{3b\pi}^{1/4}} \left[ 1 - \left( \frac{\Delta t_{kl}}{b} \right)^2 \right] e^{-\Delta t_{kl}^2/(2b^2)}, \quad (1.2)$$

where  $a$  scales the magnitude of STDP, and  $b$  scales the temporal width of the Mexican hat (see Figure 2A).

To approximate STDP in phase oscillator networks, simpler phase-dependent plasticity (PDDP) rules have been developed that prescribe synaptic changes based on differences in phase of neuron pairs rather than differences in spike timing. If the state of oscillator  $k$  is given by a phase variable  $\theta_k \in [0, 2\pi)$  on the circle, the change of coupling weight between oscillators  $k$  and  $l$  according to PDDP depends on their phase difference  $\theta_l - \theta_k$ . While symmetric STDP can be approximated by the symmetric PDDP rule originally proposed by Seliger et al. (2002), several authors added a phase-shift parameter  $\varphi$  in order to approximate causal STDP-like learning (Aoki & Aoyagi, 2009; Berner et al., 2019), as well as other types of plasticity. With this single-harmonic PDDP rule, the weight  $\kappa_{kl}$  from oscillator  $l$  to oscillator  $k$  evolves according to

$$\frac{d\kappa_{kl}}{dt} = \epsilon [\lambda \cos(\theta_l - \theta_k + \varphi) - \kappa_{kl}], \quad (1.3)$$



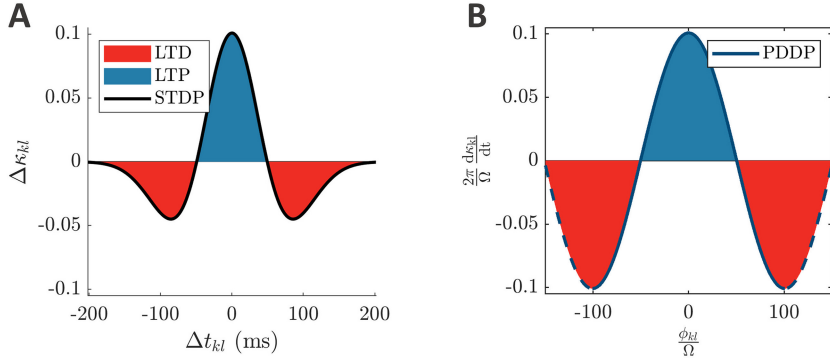


Figure 2: From symmetric STDP to single-harmonic PDDP. (A) Symmetric STDP function (Mexican hat, equation 1.2) describing the change in weight  $\Delta\kappa_{kl}$  as a function of the difference between spike times  $\Delta t_{kl}$ . (B) Considering the phase difference  $\phi_{kl} \bmod 2\pi$  instead of the difference between spike times, the STDP function in panel A can be approximated by the PDDP function in panel B (equation 1.3 with  $\varphi = 0$ ). The horizontal axis is  $\frac{\phi_{kl}}{\Omega}$ , and the vertical axis is  $\frac{2\pi}{\Omega} \frac{d\kappa_{kl}}{dt}$  to enable comparison with panel A. The solid blue line corresponds to one oscillatory period at frequency  $\Omega$  centered on  $\phi_{kl} = 0$ ; the dashed blue line extends beyond one period. The parameters used in panel A are  $a = 0.025822$ ,  $b = 0.049415$ , corresponding to  $\lambda = 1$ ,  $\epsilon = 0.5$ ,  $\Omega = 10\pi$  in panel B. LTP is highlighted in blue and LTD in red.

where  $\lambda$  controls the strength of PDDP relative to the decay of the synaptic strength and  $\epsilon$  sets the relative timescale between the plasticity mechanism and the phase dynamics. When  $\varphi = 0$ , we recover the learning rule introduced by Seliger et al., which is symmetric around a phase difference of zero. For  $\varphi = \pi/2$ , the cosine term is antisymmetric around zero, which provides a first level of approximation of additive, causal STDP (in the absence of the decay term). However, this is a coarse approximation. A PDDP rule directly based on causal STDP exponential kernels (Maistrenko et al., 2007) could be more closely related to causal STDP. Lücken et al. (2016) proposed such a rule and determined the correspondence between the parameters of the causal STDP rule, the parameters of the PDDP rule, and the parameters of the underlying network of coupled oscillators (see Figure 4B). Importantly, the synaptic strengths are continuously updated based on the evolving phase differences, while standard models of neural plasticity assume updates as discrete events when a neuron spikes.

Here, we construct mean-field approximations for coupled Kuramoto phase oscillators subject to PDDP and compare these approximations to fully adaptive networks where every edge evolves according to STDP. Specifically, we consider two types of PDDP rules: rules that update connection weights continuously, as was done in previous studies, and

event-based rules, where weights are updated according to phase differences at a particular phase corresponding to spiking. In section 2, we show that single-harmonic PDDP rules can indeed approximate symmetric STDP in adaptively coupled networks of Kuramoto oscillators, while a multiharmonic rule is required to accurately approximate causal STDP. For PDDP rules, we derive exact equations describing the evolution of the mean coupling strength in terms of the Kuramoto/Daido order parameters that encode synchrony of the oscillators' phases (see section 3). We then focus on networks with symmetric adaptive coupling that naturally form clusters (see section 2). For such networks, we construct mean-field approximations (see section 4) for the emergent coupling topologies, where each cluster corresponds to a coupled population. If we assume that coupling between clusters is through the mean coupling strength—rather than by individual weights between oscillators—we obtain low-dimensional Ott-Antonsen equations for the mean-field limit. We explicitly analyze the dynamics of the reduced equations for adaptive networks for one and two clusters. Note that these mean-field descriptions are not valid globally (i.e., there is no single reduced equation that is valid on all of state space) but rather aim to capture the dynamics on part of overall phase space determined by the initial conditions. In other words, we have a family of low-dimensional dynamics that can describe part of the phase space for this very high-dimensional system. Finally, we show that the dynamics of the full network can be approximated by such a family of low-dimensional dynamics by extracting the mean field description from the emergent clustering (see section 5). Since brain activity is transient, we focus on transients and consider additive plasticity without bounds on individual weights for causal STDP. In line with previous studies, however, we include a weight decay term when considering symmetric STDP (Seliger et al., 2002; Berner et al., 2019).

## 2 PDDP Can Approximate STDP in Kuramoto Networks

Adaptation of network connections through STDP rely—as the name suggests—on the timing of action potentials of the coupled neurons. If the state of each neuron can be described by a single phase variable (e.g., if the coupling is weak; Ashwin et al., 2016), then it may be possible to approximate STDP by an adaptation rule that depends on the phase differences between oscillators such as equation 1.3. In this section, we now consider general PDDP rules, which can update weights continuously (as in equation 1.3) or update at discrete time points (spiking events). We show that for a network of phase oscillators, these PDDP rules can approximate both symmetric and causal STDP. For causal STDP, the accuracy increases substantially as the number of harmonics in the PDDP rule is increased.

To illustrate this, we focus on the Kuramoto model (Kuramoto, 1975), which is widely used to understand synchronization phenomena in

neuroscience and beyond, subject to plasticity. Specifically, we consider  $N$  coupled Kuramoto oscillators where oscillators represent coupled neurons (Weerasinghe et al., 2019; Nguyen et al., 2020; Weerasinghe et al., 2021). The phase  $\theta_k$  of oscillator  $k$  evolves according to

$$\frac{d\theta_k}{dt} = \omega_k + \frac{1}{N} \sum_{l=1}^N \kappa_{kl} \sin(\theta_l - \theta_k) \quad (2.1)$$

with intrinsic frequency  $\omega_k$  and strength  $\kappa_{kl}$  of the synaptic connections from oscillator  $l$  to oscillator  $k$  (subject to plasticity). The (complex-valued) Kuramoto-Daido order parameters,

$$Z^{(m)} = \frac{1}{N} \sum_{k=1}^N e^{im\theta_k},$$

for  $m \in \mathbb{Z}$  capture the (cluster) synchrony of the oscillator phases. The magnitude of the first-order parameter  $Z := Z^{(1)}$ —simply called the Kuramoto order parameter—captures global synchrony, that is, for  $Z = \rho e^{i\Psi}$ , we have  $|Z| = \rho = 1$  if all oscillators have the same phase  $\theta_1 = \dots = \theta_N$ . Similarly,  $|Z^{(2)}| = 1$  if the oscillators form two antiphase clusters where  $\theta_j = \theta_k$  or  $\theta_j = \theta_k + \pi$ , and so on.

**2.1 Principles to Convert STDP to PDDP.** PDDP rules prescribe synaptic changes based on differences in phase of neuron pairs rather than differences in spike timing and can be used to approximate both symmetric and causal STDP in phase oscillator networks. In particular, the approximation is expected to hold under the assumption that the evolution of phase differences is slower than the phase dynamics (Lücken et al., 2016). Under this assumption, spike time differences are approximated by dividing phase differences by the mean angular frequency of the network  $\Omega = \frac{1}{N} \sum_{k=1}^N \omega_k$ .

As the phase difference is continuous in time, the discrete weight updates, based on spike-time differences in the case of STDP, can be converted to a continuous-time differential equation in terms of the phase differences. As a result, the coupling weight between each pair of neurons updates continuously based on the phase difference between the pre- and postsynaptic oscillators; we refer to this as continuously updating PDDP or simply PDDP when there is no ambiguity. STDP updates occur every time a neuron spikes, while PDDP updates occur continuously at every point in time. To ensure that STDP and continuously updating PDDP scale similarly, we scale the discrete STDP updates by the average number of spikes per unit time  $\Omega/2\pi$ .

Rather than updating weights continuously, we can restrict weight updates to occur only at spiking events. We say that oscillator  $k$  spikes if its phase increases through  $\theta_k = 0$ , and let  $t_k^q$  be the  $q$ th firing time of neuron  $k$ .

At each spiking event, we update the coupling weight between each pair of neurons based on their phase difference; we give explicit examples of the functional form of the updates below. We refer to this type of PDDP rule as event-based PDDP (ebPDDP). While there is an explicit phase dependence through the events, the actual change only depends on the phase difference. To ensure appropriate scaling, we again multiply by the average number of spikes per unit time and introduce an additional factor that is only nonzero when either the pre- or postsynaptic neuron spikes. This factor is defined as  $C = [\sum_q \delta(t - t_k^q) + \sum_q \delta(t - t_l^q)]/2$ , where  $\delta$  denotes the Dirac delta function.<sup>2</sup>

**2.2 Symmetric STDP and Single-Harmonic PDDP.** In this section, we show that symmetric, noncausal STDP modeled by equation 1.2 together with the weight decay  $\frac{d\kappa_{kl}}{dt} = -\epsilon\kappa_{kl}$  can be approximated by the single-harmonic PDDP learning rule introduced by Seliger et al. (2002; see equation 1.3 with  $\varphi = 0$ ). We refer to this rule in what follows as the Seliger rule. As detailed in the previous section, discrete STDP updates should be scaled by  $\Omega/2\pi$  to obtain continuous PDDP updates. Therefore, by matching the scaled maximum of equation 1.2 with the maximum of equation 1.3, we have  $[\Omega/(2\pi)] [2a/(\sqrt{3}b\pi^{1/4})] = \epsilon\lambda$ , which determines the value of  $\lambda$  for a given  $\epsilon$  (see the example in Figure 2). Moreover, to ensure that the scale of spike timing differences in the STDP rule and the scale of phase differences in the PDDP rule match without modifying the Seliger rule, we choose  $b \approx \pi/(2\Omega)$  (see Figure 2). Arbitrary values of  $b$  could be accommodated by scaling the phase difference term in the Seliger rule as detailed in the previous section. The corresponding event-based PDDP rule reads

$$\frac{d\kappa_{kl}}{dt} = \epsilon \left[ \lambda_{\text{eb}} \frac{\sum_q \delta(t - t_k^q) + \sum_q \delta(t - t_l^q)}{2} \cos(\theta_l - \theta_k) - \kappa_{kl} \right], \quad (2.2)$$

with  $\lambda_{\text{eb}} = \lambda \frac{2\pi}{\Omega}$ . Note that updates to the coupling strengths happen whenever the pre- or postsynaptic neuron spikes.

As shown in Figure 3, both single-harmonic PDDP rules (the Seliger rule and equation 2.2) can approximate symmetric STDP (equation 1.2) in networks of Kuramoto oscillators. Simulation details can be found in appendix A.1. The time evolution of the weight distribution (panel A), the coupling matrix at the last simulation time point (panel B), as well as the time evolution of the average coupling (panel C1) and network synchrony (panels C2–C3) are comparable across learning rules. In particular, the Pearson's correlation between the STDP coupling matrix and the

<sup>2</sup>The division by 2 ensures that this rule scales similarly to the STDP rule and the PDDP rule with continuous updates.

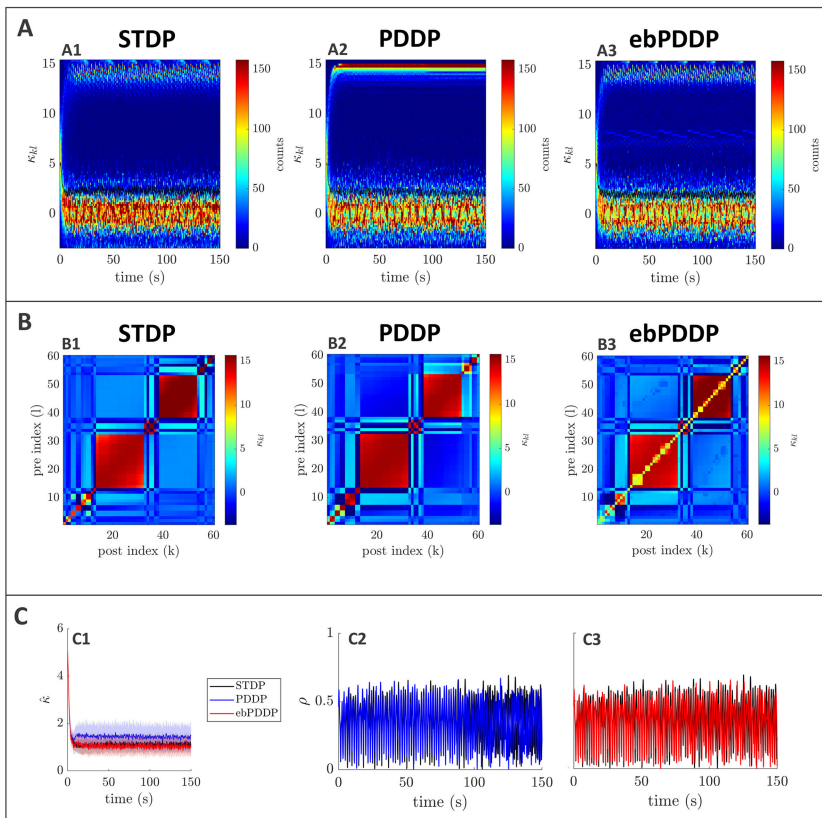


Figure 3: Comparison between symmetric STDP and PDDP in a Kuramoto network (two synchronized cluster state). (A) Evolution of the distribution of coupling weights with time (100 bins at each time point). The average weight is represented by a thin black line. STDP is shown in A1, PDDP in A2, and ebPDDP in A3. (B) Coupling matrix at  $t = 150$  s, with oscillators sorted by natural frequency. STDP is shown in panel B1, PDDP in panel B2, and ebPDDP in panel B3. (C) Time evolution of average coupling (see panel C1, where error bars represent the standard error of the mean over five repeats; the high variability is due to sensitivity to initial conditions) and network synchrony (see panels C2 and C3). STDP is shown in black, PDDP in blue, and ebPDDP in red. ( $a = 0.38733$ ,  $b = 0.049415$ ,  $\sigma_\kappa = 3$ ,  $\Delta = 1.2\pi$ ,  $\Omega = 10\pi$  (5 Hz)).

PDDP coupling matrix is 0.88, while the correlation between the STDP coupling matrix and the ebPDDP coupling matrix is 0.90. For the parameter set shown in Figure 3, we see the emergence of two synchronized clusters. For this type of dynamics, the average coupling as a function of time may be

better captured by ebPDDP than PDDP (panel C1). However, for the desynchronized state (shown in Figure 11 in appendix C), there is little difference between continuous PDDP and ebPDDP. In both states, the accuracy of the approximation could be improved by considering a Fourier expansion of the Mexican hat function rather than a single cosine term. We explore this for causal, nonsymmetric STDP in the next section, as we found that a single sine term is generally a poor approximation of the causal STDP kernel.

**2.3 Causal STDP and Multiharmonic PDDP.** In the previous section, we considered PDDP rules with a single harmonic in the phase difference. To get a better approximation of causal STDP, one can take more harmonics into account.

*2.3.1 Obtaining Multiharmonic PDDP Rules from Causal STDP.* To approximate causal STDP, we consider the PDDP rule proposed by Lücken et al. (2016) as

$$\frac{d\kappa_{kl}}{dt} = \frac{\Omega}{2\pi} \left( A_+ e^{\frac{-\phi_{kl}}{\Omega\tau_+}} - A_- e^{\frac{\phi_{kl}-2\pi}{\Omega\tau_-}} \right) = F(\phi_{kl}), \quad (2.3)$$

where  $\phi_{kl} = (\theta_l - \theta_k) \bmod 2\pi$ ,  $\Omega$  is the mean (angular) frequency of the network, and other parameters have been defined in equation 1.1. In equation 2.3, both synaptic potentiation (first term) and synaptic depression (second term) are described without requiring a piecewise definition thanks to the fast-decaying exponentials. The correspondence of this PDDP rule with additive STDP is illustrated in Figure 4B. If the postsynaptic neuron  $k$  spikes (i.e., its phase increases through 0) shortly after the presynaptic neuron  $l$ ,  $\phi_{kl}$  is small and positive, which will lead to a potentiation of  $\kappa_{kl}$ . Conversely, if the postsynaptic neuron spikes shortly before the presynaptic neuron,  $\phi_{kl} - 2\pi$  is small and negative, which will lead to a depression of  $\kappa_{kl}$ . As laid out in section 2.1, spike time differences are approximated in equation 2.3 by dividing phase differences by the network mean angular frequency. Moreover, the scaling factor  $\Omega/2\pi$  (average number of spikes per unit time) accounts for the conversion of discrete weight updates to a continuous-time differential equation. The corresponding event-based PDDP rule can be obtained as

$$\begin{aligned} \frac{d\kappa_{kl}}{dt} &= \frac{\sum_q \delta(t - t_k^q) + \sum_q \delta(t - t_l^q)}{2} \left( A_+ e^{\frac{-\phi_{kl}}{\Omega\tau_+}} - A_- e^{\frac{\phi_{kl}-2\pi}{\Omega\tau_-}} \right), \\ &= \frac{\pi}{\Omega} \left( \sum_q \delta(t - t_k^q) + \sum_q \delta(t - t_l^q) \right) F(\phi_{kl}), \end{aligned} \quad (2.4)$$

where  $F$  is given by equation 2.3.

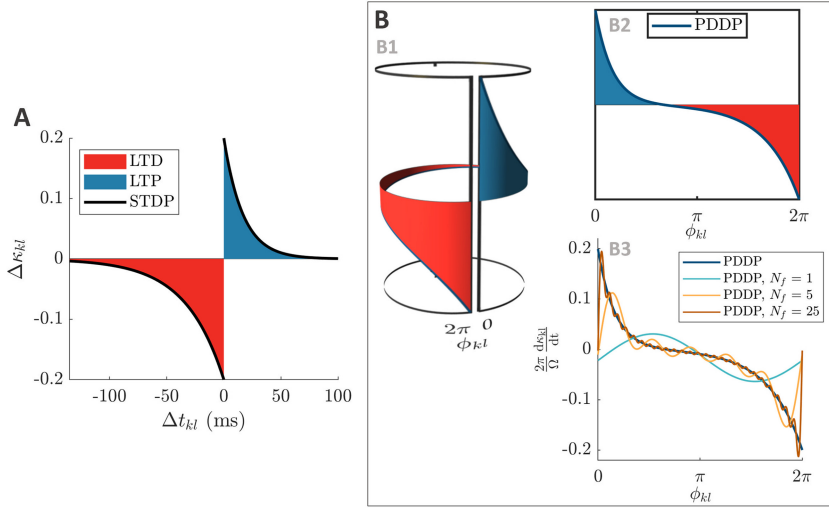


Figure 4: From causal STDP to multiharmonic PDDP. (A) STDP function (equation 1.1) describing the change in weight  $\Delta\kappa_{kl}$  as a function of the difference between spikes times  $\Delta t_{kl}$ . (B) Considering the phase difference  $\phi_{kl}$  mod  $2\pi$  instead of the difference between spike times, the STDP function in panel A can be approximated by the PDDP function in panel B2 (equation 2.3). As shown in panel B1, wrapping the PDDP function around a cylinder to join  $\phi_{kl} = 0$  and  $\phi_{kl} = 2\pi$  illustrates the correspondence with the STDP function. In panel B3, the PDDP function is approximated using truncated Fourier series with 1, 5, and 25 Fourier components. The vertical axis is  $\frac{2\pi}{\Omega} \frac{d\kappa_{kl}}{dt}$  to enable comparison with panel A. The parameters used in all panels are  $\tau_+ = 16.8$  ms and  $\tau_- = 33.7$  ms,  $A_+ = A_- = 0.2$ . LTP is highlighted in blue and LTD in red.

In both cases, we can expand  $F(\phi_{kl})$  as a Fourier series of the phase difference since  $\phi_{kl}$  is defined modulo  $2\pi$ , which makes  $F(\phi_{kl})$  a  $2\pi$ -periodic function. The Fourier expansion will be key to deriving the evolution of the average coupling strength in section 3 and can be truncated to include only  $N_f$  components for simulations (see the examples in Figure 4C). We note that the PDDP rule by Berner et al. (2019) with  $\varphi \approx \pi/2$  is a single-harmonic version of the rule by Lücken et al. (2016, with a vertical shift), and call truncated Fourier expansions of equations 2.3 and 2.4 with  $N_f > 1$  “multiharmonic PDDP.” We express the Fourier series of  $F$  as

$$\begin{aligned}
 F(\phi_{kl}) &= \sum_{m=-\infty}^{\infty} c_m e^{mi(\theta_l - \theta_k)} \\
 &= \frac{a_0}{2} + \sum_{m=1}^{\infty} [a_m \cos\{m(\theta_l - \theta_k)\} + b_m \sin\{m(\theta_l - \theta_k)\}], \quad (2.5)
 \end{aligned}$$



where  $(c_m)_{m \in \mathbb{Z}}$  are the complex-valued Fourier coefficients, or equivalently  $(a_m)_{m \in \mathbb{N}}$ , and  $(b_m)_{m \in \mathbb{N}^*}$  are the real-valued Fourier coefficients. The Fourier coefficients only depend on the parameters of the STDP rule, equation 1.1, and  $\Omega$ , and the real-valued coefficients can be obtained analytically as

$$\begin{aligned} a_m &= \frac{1}{\pi} \int_0^{2\pi} F(x) \cos(mx) dx \\ &= \frac{\Omega}{2\pi^2} \left[ \frac{A_+ \tau_+}{1 + m^2 \tau_+^2} \left( 1 - e^{-\frac{2\pi}{\tau_+}} \right) + \frac{A_- \tau_-}{1 + m^2 \tau_-^2} \left( e^{-\frac{2\pi}{\tau_-}} - 1 \right) \right], \\ b_m &= \frac{1}{\pi} \int_0^{2\pi} F(x) \sin(mx) dx \\ &= \frac{\Omega}{2\pi^2} \left[ \frac{mA_+ \tau_+^2}{1 + m^2 \tau_+^2} \left( 1 - e^{-\frac{2\pi}{\tau_+}} \right) + \frac{mA_- \tau_-^2}{1 + m^2 \tau_-^2} \left( 1 - e^{-\frac{2\pi}{\tau_-}} \right) \right]. \end{aligned} \quad (2.6)$$

**2.3.2 Comparison of Learning Rules.** Multiharmonic PDDP can approximate causal STDP in Kuramoto networks (simulation details can be found in appendix A.2). As the number of harmonics included in the PDDP rules is increased, the dynamics for the networks with PDDP begin to match those of the STDP network (see Figure 5). The time evolution of the weight distribution (panel A), the coupling matrix at the last simulation time point (panel B), as well as the time evolution of the average coupling (panel C1) and network synchrony (panels C2 to C7) are closely matched for causal STDP and multiharmonic PDDP or ebPDDP when enough Fourier components are included ( $N_f = 25$ ). Simulations were also performed for a range of parameter values, and the findings were similar (see Figures 12 to 15 in appendix C). Single-harmonic PDDP or ebPDDP ( $N_f = 1$ ) can provide a first level of approximation of causal STDP in certain cases when the time evolution of the weight distribution is simple (see Figure 14). However, single-harmonic rules are unable to describe more complex cases, even qualitatively (as seen in Figure 5). In all cases studied for a network frequency of 5 Hz, 25 Fourier components are deemed sufficient to approximate the dynamics of the network with causal STDP. While the performance of ebPDDP is similar to PDDP, ebPDDP is slightly more accurate than PDDP. To quantitatively compare STDP to PDDP and ebPDDP, we construct error metrics for the time evolution of the weight distribution  $e_{\text{hist}(\kappa_{kl})}$ , the average coupling  $e_{\hat{\kappa}}$ , and the network synchrony  $e_{\rho}$ , and consider the Pearson's correlation between coupling matrices at the last simulation time point  $r_{\kappa_{kl}}^{\infty}$ . These metrics are defined in appendix A.2. In general, these metrics improve with increasing  $N_f$  (see Figure 6A), although stagnation or a slight worsening can be seen when the error is already low. Though it is of no consequence in Kuramoto networks with sine coupling, self-coupling weights are consistently different between causal STDP and multiharmonic PDDP

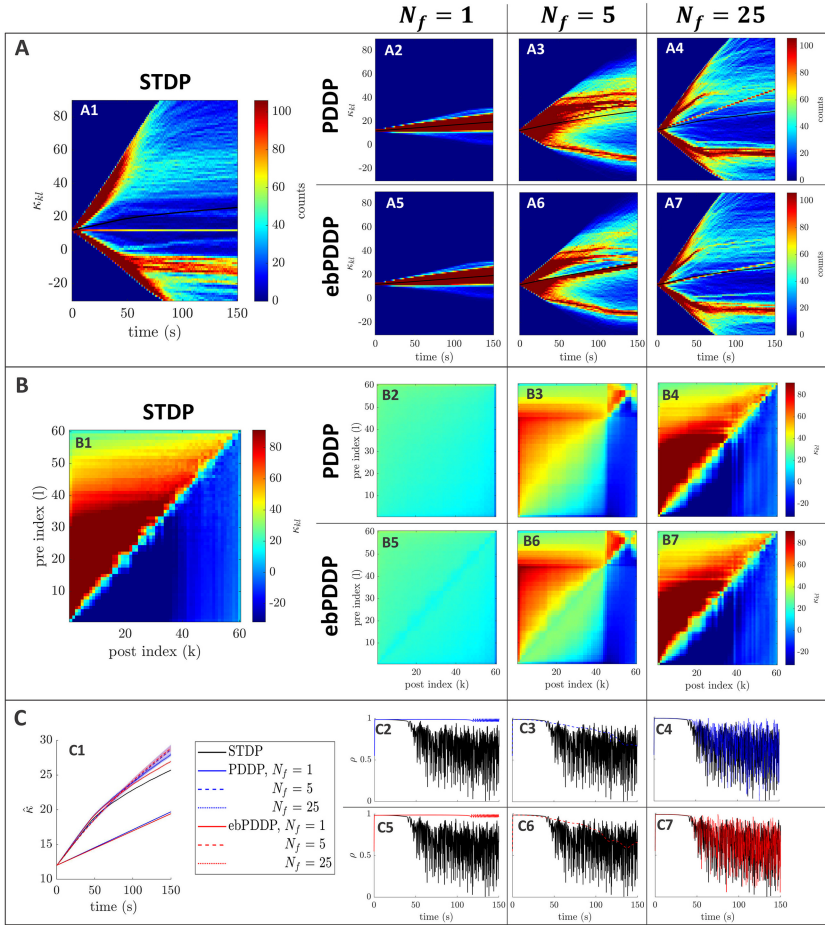


Figure 5: Comparison between STDP and PDDP in a Kuramoto network ( $\beta = 0.5$ ,  $\sigma_\kappa = 0.2$ ,  $\Delta = 0.6\pi$ ,  $\Omega = 10\pi$  (5 Hz)). Results for PDDP and ebPDDP are shown for 1, 5, and 25 Fourier components  $N_f$  (first, second, and third columns on the right-hand side of the figure, respectively). (A) Evolution of the distribution of coupling weights with time (100 bins at each time point). The average weight is represented by a thin black line. STDP is shown in panel A1, PDDP in panels A2 to A4, and ebPDDP in panels A5 to A7. (B) Coupling matrix at  $t = 150$  s, with oscillators sorted by natural frequency. STDP is shown in panel B1, PDDP in panels B2 to B4, and ebPDDP in panels B5 to B7. (C) Time evolution of average coupling (in panel C1, error bars represent the standard error of the mean over five repeats) and network synchrony (panels C2 to C7). STDP is shown in black, PDDP in blue, and ebPDDP in red. In all panels, the approximation becomes better as  $N_f$  is increased.

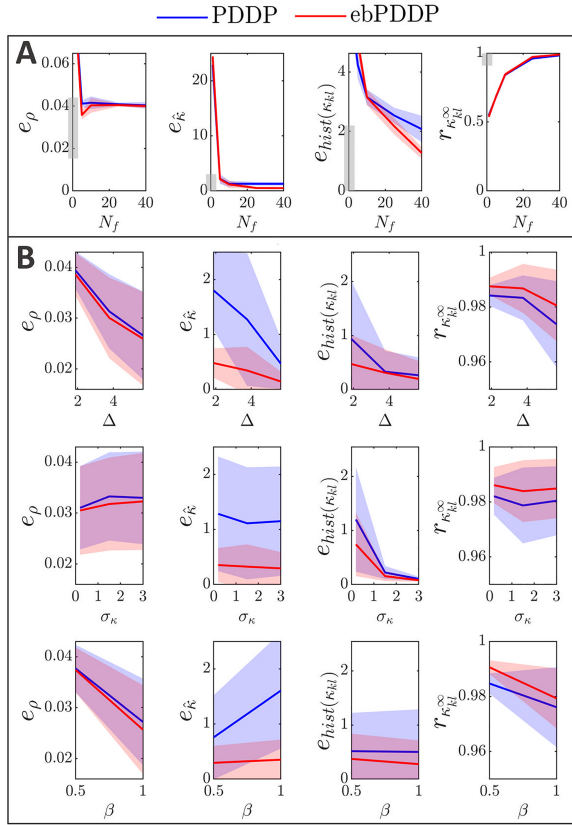


Figure 6: Influence of  $N_f$ ,  $\Delta$ ,  $\sigma_\kappa$ , and  $\beta$  on error metrics. Error metrics for PDDP compared to STDP for the time evolution of network synchrony  $e_\rho$ , average coupling  $e_{\hat{\kappa}}$  and distribution of weights  $e_{\text{hist}(\kappa_{kl})}$ , and for the coupling matrix at the last stimulation point  $r_{\kappa_{kl}}^\infty$  are shown in the first, second, third, and fourth columns, respectively. Results for PDDP are in blue and for ebPDDP in red. (A) Influence of the number of Fourier coefficients  $N_f$  on the error metrics for the parameters used in Figure 5 ( $\beta = 0.5$ ,  $\sigma_\kappa = 0.2$ ,  $\Delta = 0.6\pi$ ,  $\Omega = 10\pi$ ). Error bars show the standard error of the mean (sem) over five repeats. (B) Influence of the network parameters on the error metrics for  $N_f = 40$ . The standard deviation of the oscillator frequency distribution  $\Delta$  is shown in the first row, the standard deviation of the initial weight distribution  $\sigma_\kappa$  is given in the second row, and the ratio for the LTP to LTD scaling factors  $\beta$  is depicted in the third row. All combinations of parameters  $\Delta = \{0.6\pi, 1.2\pi, 1.8\pi\}$ ,  $\sigma_\kappa = \{0.2, 1.5, 3\}$ ,  $\beta = \{0.5, 1\}$  are included with five repeats for each combination. In each row, averaging is performed over the parameters that do not correspond to the horizontal axis (standard deviation error bars). Note that the scale of the vertical axes is 2 to 10 times smaller than in panel A for readability (range indicated by gray bars). See Figure 19 for detailed slices in parameter space.

or ebPDDP in our simulations. This is due to the truncated Fourier expansions of  $F$  not being zero when the phase difference is zero (see Figure 4B3).

**2.3.3 Parameter Dependence.** Model parameters influence the four metrics described in the previous section (see Figure 6B), although the impact on  $r_{\kappa_{kl}}^\infty$  is minor (always stays  $> 0.96$ ). Increasing the standard deviation of the frequency distribution ( $\Delta$ ) tends to improve the error metrics, except  $r_{\kappa_{kl}}^\infty$ , which gets slightly lower. This is expected since a larger  $\Delta$  reduces synchrony and makes the weight distribution more unimodal. The impact of the standard deviation of the initial coupling distribution ( $\sigma_\kappa$ ) on the metrics is smaller, except for the time evolution of the weight distribution. The effect of the ratio of the scales of LTD to LTP ( $\beta = A_-/A_+$ ) depends on the metric considered. The largest effect is a lowering of  $e_\rho$  when LTD dominates ( $\beta = 1$ ) compared to the balanced situation ( $\beta = 0.5$ ). This is due to the fact that the time evolution of  $\rho$  is closely approximated with  $N_f = 1$  when LTD dominates, whereas in the balanced state, more Fourier components are required to obtain a good approximation. Since dominant LTD leads to lower synchrony, this matches the previous observation that lower synchrony is associated with lower error metrics. Time courses of  $\rho$  for both states can be found in appendix C; Figure 12 shows the balanced state, and Figure 14 shows the LTD dominant regime.

To test the robustness of our findings, we studied a network with a mean frequency four times higher (20 Hz) and considered the least favorable part of parameter space (lowest  $\Delta$ , lowest  $\sigma_\kappa$ , and  $\beta = 0.5$ ) (see Figure 15 in appendix C). The order of magnitude of the error metrics is the same as for 5 Hz, except for  $r_{\kappa_{kl}}^\infty$  (see Figure 18C in appendix C). The lower value for  $r_{\kappa_{kl}}^\infty$  may be explained by the greater complexity and finer structures in the coupling matrix. However, the coupling matrix obtained at the last stimulation point with multiharmonic ebPDDP for  $N_f = 75$  (see Figure 15 in appendix C, panel B7) is qualitatively very similar to the coupling matrix obtained with STDP (see panel B1). At 20 Hz, the period of the oscillators is comparable to the STDP time constants; hence, the weight distribution patterns unfolding in time are more highly multimodal than at 5 Hz. These patterns are still well approximated by multiharmonic PDDP and ebPDDP, but a larger number of Fourier components than at 5 Hz is warranted for accurate results. Simulating this higher-frequency network required a smaller simulation time step ( $\Delta t = 0.1$  ms). However, the time step has overall little impact on the error metrics at lower frequencies (see Figure 18 in appendix C, panel B).

Additional explorations of the parameter dependencies can be found in Figures 18 and 19 in appendix C.

### 3 Evolution of the Average Coupling Strength in Networks with PDDP

While each coupling weight  $\kappa_{kl}$  evolves independent of one another, we now derive evolution equations for the average coupling weight

$$\hat{\kappa} = \frac{1}{N^2} \sum_{k=1}^N \sum_{l=1}^N \kappa_{kl} \quad (3.1)$$

for both continuously updating and event-based PDDP. Obtaining the mean coupling weight dynamics is necessary for constructing our mean-field approximations, which are based on the average coupling weights within and between populations.

**3.1 Average Coupling for General PDDP.** Suppose that each weight  $\kappa_{kl}$  evolves according to a general, continuously updating PDDP rule  $\frac{d\kappa_{kl}}{dt} = F(\phi_{kl})$ , where  $F$  is a  $2\pi$ -periodic function of the phase difference  $\phi_{kl}$ . The PDDP rule in section 2.3 with  $F$  approximating causal STDP (see equation 2.3) is a particular example. Writing  $F(\phi_{kl}) = \sum_{m=-\infty}^{\infty} c_m e^{mi(\theta_l - \theta_k)}$  as in equation 2.5 and differentiating equation 3.1 yields

$$\frac{d\hat{\kappa}}{dt} = \sum_{m=-\infty}^{\infty} \frac{c_m}{N^2} \sum_{k=1}^N \sum_{l=1}^N e^{mi\theta_l} e^{-mi\theta_k}. \quad (3.2)$$

This expression can be written in terms of the Kuramoto-Daido order parameters  $Z^{(m)}$ . We have  $Z^{(-m)} = \bar{Z}^{(m)}$  and consequently equation 3.2 reads

$$\frac{d\hat{\kappa}}{dt} = \sum_{m=-\infty}^{\infty} c_m Z^{(m)} \bar{Z}^{(m)} = \sum_{m=-\infty}^{\infty} c_m |Z^{(m)}|^2.$$

The series converges as  $|Z^{(m)}| \leq 1$  and the Fourier series of  $F$  is assumed to converge. Since  $c_m + c_{-m} = a_m$  and  $2c_0 = a_0$ , the evolution equation for  $\hat{\kappa}$  can be simplified to

$$\frac{d\hat{\kappa}}{dt} = \frac{a_0}{2} + \sum_{m=1}^{\infty} a_m |Z^{(m)}|^2. \quad (3.3)$$

In the case of  $F$  approximating causal STDP, the coefficients  $(a_m)_{m \in \mathbb{N}}$  are given by equation 2.6. In the absence of bounds on the coupling weights, equation 3.3 exactly describes the average coupling strength in a phase oscillator network with PDDP, as illustrated in Figure 7.

If the PDDP rule contains a decay term, the evolution of the mean coupling strength will reflect this as well. More concretely, consider an evolution of individual coupling weights  $\frac{d\kappa_{kl}}{dt} = \epsilon [\lambda F(\phi_{kl}) - \kappa_{kl}]$  as in the PDDP

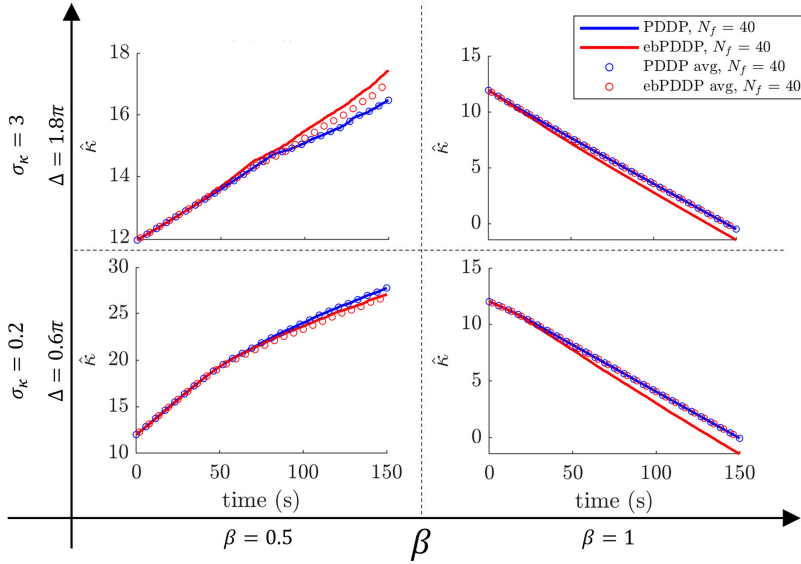


Figure 7: Simulation of average coupling rules in Kuramoto networks. Equation 3.3 (blue circles) describes exactly the average coupling weight in Kuramoto networks with PDDP (blue lines). The correspondence between equation 3.6 (red circles) and the average coupling weight in Kuramoto networks with ebPDDP (equation 2.4, red lines) is not exact, as explained in the main text. The same numbers of Fourier components are used in all cases ( $N_f = 40$ ). The four sets of parameters used for the simulations are indicated by the bold axes and correspond to those used in Figure 5, as well as Figures 12, 13, and 14 in appendix C.

rule by Seliger et al. (2002) where  $\lambda$  and  $\epsilon$  are parameters. Then the evolution of the average coupling is

$$\frac{d\hat{k}}{dt} = \epsilon \left[ \lambda \left( \frac{a_0}{2} + \sum_{m=1}^{\infty} a_m |Z^{(m)}|^2 \right) - \hat{k} \right]. \quad (3.4)$$

In particular, for  $a_1 = \cos(\varphi)$  and all other Fourier coefficients equal to zero, this equation exactly describes the evolution of the average coupling for the PDDP rule given by equation 1.3.

**3.2 Average Coupling for General Event-Based PDDP.** We consider the general ebPDDP rule represented by equation 2.4 where  $F$  is any  $2\pi$ -periodic function of the phase difference that can be expanded as a Fourier series according to equation 2.5. To obtain the corresponding average coupling strength, the Dirac deltas indicating spiking events need to be

expressed as functions of a neuron's phases. Since  $\theta_k$  is defined mod  $2\pi$ , we have  $\sum_q \delta(t - t_k^q) \approx \Omega \delta(\theta_k)$  as in Coombes & Byrne (2019). We use this approximation to define an ebPDDP rule that depends only on the phases of the oscillators:

$$\frac{d\kappa_{kl}}{dt} = \pi (\delta(\theta_k) + \delta(\theta_l)) F(\phi_{kl}). \quad (3.5)$$

Using the Fourier expansion of  $F$  as before, the corresponding average coupling  $\hat{\kappa}$  can be obtained as

$$\frac{d\hat{\kappa}}{dt} = \pi \sum_{m=-\infty}^{\infty} \frac{c_m}{N^2} \sum_{k=1}^N \sum_{l=1}^N (e^{mi\theta_l} \delta(\theta_k) e^{-mi\theta_k} + e^{-mi\theta_k} \delta(\theta_l) e^{mi\theta_l}).$$

With  $\theta$  defined mod  $2\pi$ ,  $\delta(\theta)$  can also be Fourier-expanded as  $\delta(\theta) = \frac{1}{2\pi} \sum_{p \in \mathbb{Z}} e^{pi\theta}$  (Coombes & Byrne, 2019). Since

$$\begin{aligned} \frac{1}{N} \sum_{k=1}^N \delta(\theta_k) e^{\pm mi\theta_k} &= \frac{1}{2\pi N} \sum_{k=1}^N \sum_{p \in \mathbb{Z}} e^{(p \pm m)i\theta_k} \\ &= \frac{1}{2\pi} \sum_{p \in \mathbb{Z}} \frac{1}{N} \sum_{k=1}^N e^{pi\theta_k} = \frac{1}{2\pi} \sum_{p \in \mathbb{Z}} Z^{(p)}, \end{aligned}$$

we obtain

$$\begin{aligned} \frac{d\hat{\kappa}}{dt} &= \left( \frac{1}{2} \sum_{p \in \mathbb{Z}} Z^{(p)} \right) \sum_{m=-\infty}^{\infty} c_m (Z^{(m)} + \bar{Z}^{(m)}) \\ &= \left( 1 + 2 \sum_{p=1}^{\infty} \operatorname{Re}(Z^{(p)}) \right) \sum_{m=-\infty}^{\infty} c_m \operatorname{Re}(Z^{(m)}). \end{aligned}$$

Using the real-valued Fourier coefficients defined in equation 2.6, this expression becomes

$$\frac{d\hat{\kappa}}{dt} = \left( 1 + 2 \sum_{p=1}^{\infty} \operatorname{Re}(Z^{(p)}) \right) \left( \frac{a_0}{2} + \sum_{m=1}^{\infty} a_m \operatorname{Re}(Z^{(m)}) \right). \quad (3.6)$$

As in section 3.1, this result can be extended to include a decay term.

Simulations show that average weights obtained from equation 3.6 are similar to average weights obtained from equation 2.4 as shown in Figure 7. Although equation 3.6 is an exact description of the average weight in phase oscillator networks with adaptivity given by equation 3.5 (where



the Dirac deltas are functions of phase), our simulations are based on equation 2.4 (where the Dirac deltas are functions of time). The approximation  $\sum_q \delta(t - t_k^q) \approx \Omega \delta(\theta_k)$  used to derive equation 3.5 from equation 2.4 gives rise to the discrepancies visible in Figure 7.

#### 4 Mean-Field Dynamics of Oscillator Populations with Adaptive Coupling

Symmetric or nearly symmetric STDP rules can lead to the formation of densely connected clusters with homogeneous coupling strength (see section 2.2 and, for example, Popovych et al., 2015; Berner et al., 2019; Röhr et al., 2019). Specifically, Figure 3 shows the emergence of multiple clusters of distinct mean intrinsic frequencies. For the remainder we will focus on such plasticity rules and interpret each cluster as an emergent population of phase oscillators. Suppose that there are  $M$  emergent clusters and the corresponding populations  $\mu \in \{1, \dots, M\}$  have  $N_\mu$  oscillators. Rewriting equation 2.1 with the cluster labeling, the evolution of  $\theta_{\mu,k}$ , the phase of oscillator  $k \in \{1, \dots, N_\mu\}$  in cluster  $\mu$  is given by

$$\dot{\theta}_{\mu,k} = \omega_{\mu,k} + \frac{1}{N} \sum_{v=1}^M \sum_{l=1}^{N_v} \kappa_{\mu v,kl} \sin(\theta_{v,l} - \theta_{\mu,k}), \quad (4.1)$$

where  $\kappa_{\mu v,kl}$  is the coupling strength from oscillator  $l$  in population  $v$  to oscillator  $k$  in population  $\mu$ . We now suggest a low-dimensional description of the resulting dynamics for populations corresponding to emergent clusters in the fully adaptive network in terms of the population Kuramoto-order parameters  $Z_\mu := \frac{1}{N_\mu} \sum_{k=1}^{N_\mu} e^{i\theta_k}$ .

**4.1 Low-Dimensional Dynamics for Homogeneous Coupling.** Using the assumption that the emergent coupling within and between clusters is homogeneous, we replace individual coupling strengths  $\kappa_{\mu v,kl}$  from oscillators in population  $v$  to oscillators in population  $\mu$  by the mean coupling strength from population  $v$  to population  $\mu$ :

$$\hat{\kappa}_{\mu v} = \frac{1}{N_\mu N_v} \sum_{k=1}^{N_\mu} \sum_{l=1}^{N_v} \kappa_{\mu v,kl}. \quad (4.2)$$

Writing  $q_\mu = \frac{N_\mu}{N}$  for the relative population size, we obtain

$$\dot{\theta}_{\mu,k} = \omega_{\mu,k} + \sum_{v=1}^M \frac{q_v}{N_v} \hat{\kappa}_{\mu v} \sum_{l=1}^{N_\mu} \sin(\theta_{v,l} - \theta_{\mu,k}), \quad (4.3)$$

which describes homogeneously coupled populations.

Such networks of Kuramoto oscillators admit an exact low-dimensional description in terms of the dynamics of the population order parameter  $Z_\mu$  due to the Ott-Antonsen reduction (Ott & Antonsen, 2008, 2009; see also Bick et al., 2020). In the mean-field limit of infinitely large networks, the Kuramoto-Daido order parameters  $Z_\mu^{(m)}$  for each population  $\mu$  describe the distribution of oscillators. The key observation for this reduction is that for networks of the form equation 4.3 the  $m$ th Kuramoto-Daido order parameter can be expressed as a power of the Kuramoto-order parameter  $Z_\mu := Z_\mu^{(1)}$ , that is,  $Z_\mu^{(m)} = (Z_\mu^{(1)})^m = Z_\mu^m$ . If we assume that the intrinsic frequencies  $\omega_{\mu,k}$  are distributed according to a Lorentzian with mean  $\Omega_\mu$  and width  $\Delta_\mu$ , then the dynamics of equation 4.3 are determined by

$$\frac{dZ_\mu}{dt} = (-\Delta_\mu + i\Omega_\mu)Z_\mu + \frac{1}{2} \sum_{v=1}^M q_v \hat{\kappa}_{\mu v} (Z_v - \bar{Z}_v Z_\mu^2). \quad (4.4)$$

The dynamical equations for the evolving coupling weights can be derived as in section 3 and then taking the limit  $N \rightarrow \infty$ . Now the Ott-Antonsen reduction allows us to simplify the expressions through  $Z_\mu^{(m)} = Z_\mu^m$ . If individual weights evolve according to the general PDDP rule  $\frac{d\kappa_{v\mu,jk}}{dt} = F(\theta_{v,j} - \theta_{\mu,k})$ , then

$$\frac{d\hat{\kappa}_{\mu v}}{dt} = \sum_{m=-\infty}^{\infty} c_m Z_\mu^m \bar{Z}_v^m. \quad (4.5)$$

Similarly, for the event-based rule (see equation 3.5) we note that  $(\sum_{p \in \mathbb{Z}} Z_\mu^{(p)}) = \frac{1 - |Z_\mu|^2}{1 - Z_\mu - \bar{Z}_\mu + |Z_\mu|^2} =: f(Z_\mu)$  and thus

$$\frac{d\hat{\kappa}_{\mu v}}{dt} = \sum_{m=-\infty}^{\infty} c_m (f(Z_\mu) Z_\mu^m + f(Z_v) \bar{Z}_\mu^m). \quad (4.6)$$

Decay terms can be incorporated in the same way as above.

Note that equation 4.4 together with either equation 4.5 or 4.6 form a closed set of equations. In the following, we analyze the dynamics of the reduced equations explicitly. Here, we focus on the symmetric STDP rule approximated by a single harmonic PPDP rule, equation 1.3, with  $\varphi = 0$  such that

$$\frac{d\hat{\kappa}_{\mu v}}{dt} = \epsilon (\lambda \operatorname{Re}(Z_\mu \bar{Z}_v) - \hat{\kappa}_{\mu v}). \quad (4.7)$$

Equations 4.4 and 4.7 now form a closed low-dimensional system of coupled adaptive oscillator populations. While these equations can be analyzed

explicitly—as we will do in the following sections—some insights have been obtained using geometric singular perturbation theory for a very small time-scale separation parameter  $\epsilon$  (<https://arxiv.org/pdf/2301.07071.pdf>).

**4.2 Single Harmonic PDDP, One Population.** We begin by considering a one-population model to illustrate the types of behavior possible for a one-cluster state. For a one-population model, the learning rule equation 4.7 does not depend on the mean phase. Thus, the phase dynamics decouple, leading to two-dimensional effective dynamics<sup>3</sup> determined by

$$\frac{d\hat{\kappa}}{dt} = \epsilon [\lambda \rho^2 - \hat{\kappa}], \quad (4.8)$$

$$\frac{d\rho}{dt} = \left( -\Delta + \frac{1}{2}\hat{\kappa} - \frac{1}{2}\hat{\kappa}\rho^2 \right) \rho, \quad (4.9)$$

where  $\rho := |Z|$ . Note that in contrast to mean-field descriptions of Kuramoto oscillators with an adaptive global coupling parameter that depend linearly on the mean field  $Z$  (Ciszak et al., 2020), we here have a quadratic dependency.

There is a trivial fixed point at  $\hat{\kappa} = 0, \rho = 0$ . While  $\hat{\kappa} = \lambda \rho^2, \rho = \sqrt{1 - \frac{2\Delta}{\hat{\kappa}}}$  defines a pair of nontrivial fixed points, which exist for  $\lambda > 8\Delta$ . Computing the Jacobian, we find that the trivial solution is stable for all physical parameter values ( $\Delta > 0, \epsilon > 0$ ), and for the nontrivial fixed points, one is stable and the other unstable.

Using XPPAUT (Ermentrout, 2002), we performed a one-parameter continuation in the heterogeneity parameter  $\Delta$  (see Figure 8). When the heterogeneity is low, there exists a nontrivial stable fixed point, where the mean coupling does not decay to zero, whereas after the saddle-node bifurcation at  $\Delta = 0.125$ , the mean coupling will always decay to zero and the oscillators will be asynchronous ( $\rho = 0$ ). As the strength of the plasticity rule  $\lambda$  is increased, the saddle node moves to the right, and the region of bistability (where the trivial and non-trivial fixed points coexist) increases. These results agree with analytical results outlined above.

**4.3 Single Harmonic PDDP, Two Populations.** Next consider two adaptively coupled populations evolving according to

$$\begin{aligned} \frac{dZ_1}{dt} = & (-\Delta + i\Omega)Z_1 + \frac{1}{2}q\hat{\kappa}_{11}Z_1(1 - |Z_1|^2) \\ & + \frac{1}{2}(1 - q)\hat{\kappa}_{12}(Z_2 - \bar{Z}_2Z_1^2), \end{aligned} \quad (4.10)$$

<sup>3</sup>Note that equilibrium points of the effective dynamics correspond to periodic solutions of the full system.

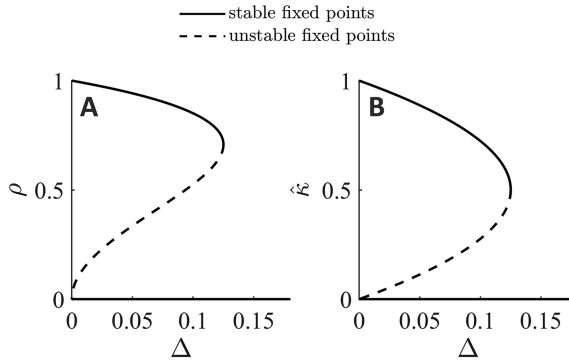


Figure 8: Bifurcation analysis of the mean-field equations for a single population. One parameter continuation in the heterogeneity parameter  $\Delta$  for equations 4.8 and 4.9 with  $\lambda = 1$  and  $\epsilon = 0.5$ . A saddle-node bifurcation occurs at  $\Delta = 0.125$ , which corresponds to the analytical value  $\lambda/8$ .

$$\begin{aligned} \frac{dZ_2}{dt} = & (-\Delta + i[\Omega + \Delta\Omega])Z_2 + \frac{1}{2}q\hat{k}_{21}(Z_1 - \bar{Z}_1Z_2^2) \\ & + \frac{1}{2}(1-q)\hat{k}_{22}Z_2(1 - |Z_2|^2), \end{aligned} \quad (4.11)$$

where  $q$  is the fraction of oscillators in population 1 and  $\Delta\Omega$  is the difference in mean intrinsic frequency between oscillators in each population. The dynamics for the intrapopulation coupling are as in the one-population model,

$$\frac{d\hat{k}_{\mu\mu}}{dt} = \epsilon [\lambda|Z_\mu|^2 - \hat{k}_{\mu\mu}], \quad (4.12)$$

for  $\mu \in [1, 2]$ , while the interpopulation coupling is given by equation 4.7.

Setting  $q = 0.5$  (two equally sized populations), we perform a one-parameter continuation in the intrinsic frequency difference  $\Delta\Omega$  (see Figure 9A). We find that for a small range of  $\Delta\Omega$  values ( $\Delta\Omega \in [-0.23, 0.23]$ ) the two populations synchronize in frequency. This frequency-locked solution lies on an invariant set, where the level of synchrony of each population is identical ( $\rho_1 = \rho_2$ ) and the coupling strengths are symmetric ( $\hat{k}_{11} = \hat{k}_{22}$ ,  $\hat{k}_{12} = \hat{k}_{21}$ ). The system itself, however, is generally not symmetric (unless  $\Delta\Omega = 0$ ) due to distinct intrinsic frequencies resulting in distinct mean phases of the two populations. The two nontrivial equilibrium branches in the interpopulation coupling strength (see Figure 9, panel A3), correspond to the in-phase/symmetric solution (positive  $\hat{k}_{\mu\nu}$ ) and the antiphase/asymmetric solution (negative  $\hat{k}_{\mu\nu}$ ).

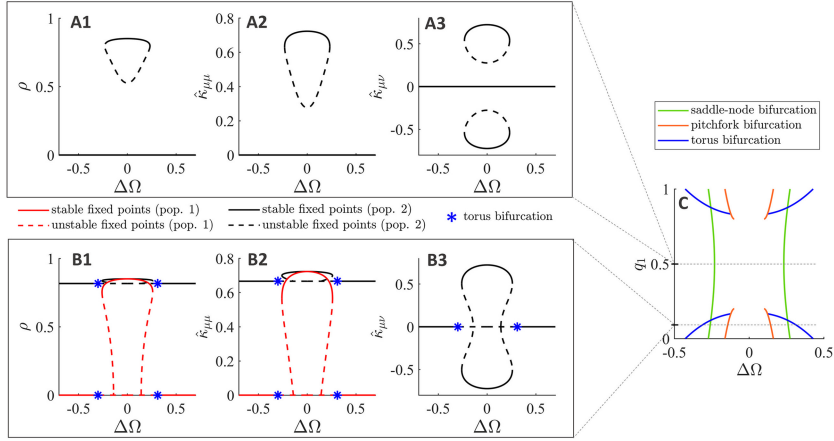


Figure 9: Bifurcation analysis of the mean-field equations for a two-population model. One- and two-parameter continuations for the system of equations given by equations 4.10 to 4.12 and 4.7. (A) One-parameter continuation in intrinsic frequency difference  $\Delta\Omega$  for equally sized populations ( $q = 0.5$ ). Given the symmetry in the system, both populations have the same within-population synchrony and intra-/interpopulation coupling strengths. Black solid (dashed) lines correspond to the stable (unstable) fixed-point values for both populations/sets of coupling strengths. (B) Continuation in  $\Delta\Omega$  for  $q = 0.1$ . As the mean interpopulation coupling strengths are equal, the curve in panel B3 corresponds to both  $\hat{k}_{12}$  and  $\hat{k}_{21}$ . (C) Two-parameter continuation in the intrinsic frequency difference  $\Delta\Omega$  and the relative size of population 1  $q$ , showing the saddle-node, pitchfork, and torus bifurcation curves. Parameter values:  $\Delta = 0.1$ ,  $\Omega = 30$ ,  $\epsilon = 0.5$ ,  $\lambda = 1$ .

For general population sizes  $q$ , an additional branch of solution can emerge, where one population is fully asynchronous and the other is partially synchronized with nontrivial dynamics (e.g.,  $\rho_1 = 0$ ,  $\rho_2 \neq 0$ ); we call this the *decoupled solution*. More specifically, the structure of the equations implies that  $\rho_1 = \hat{k}_{12} = \hat{k}_{21} = 0$  defines a dynamically invariant set. On this set, the coupling strength  $\hat{k}_{11}$  decays exponentially, and the second population evolves independent of the first one (as the network is decoupled) according to the equations of motion for a single population with adaptive coupling. The decoupled solution now corresponds to the nontrivial solution branch for a single population (see Figure 8), which exists for  $\lambda > 8\Delta$ . The only difference here is that the coupling  $\hat{k}$  is replaced by an effective coupling  $q_\mu \hat{k}_{\mu\mu}$  scaled with the (relative) population size. Hence, decoupled solutions exist only for  $q < 2\Delta/\lambda$  (population 2 has nontrivial dynamics  $\rho_2 \neq 0$ ) and  $q > 8\Delta/\lambda$  (population 1 has nontrivial dynamics  $\rho_1 \neq 0$ ). Note that these are equilibrium points for the effective dynamics but periodic solutions in the full system.

Letting  $q = 0.1$ , we find and continue the decoupled solution where population 1 is asynchronous and population 2 has nontrivial dynamics ( $\rho_1 = 0$ ,  $\rho_2 \neq 0$ ) (see Figure 9B). The dynamics of population 1 (population 2) is shown in red (black). The interpopulation coupling strengths are equal for all values of  $\Delta\Omega$ . Hence, the curve in Figure 9, panel B3 corresponds to  $\hat{\kappa}_{12}$  and  $\hat{\kappa}_{21}$ . The decoupled solution goes unstable at a torus bifurcation (blue stars)  $\Delta\Omega \approx -0.3$  and restabilizes at a second torus bifurcation at  $\Delta\Omega \approx 0.3$ . The frequency-locked solution branches off the decoupled solution at a pitchfork bifurcation at  $\Delta\Omega \approx -0.15$  and  $\Delta\Omega \approx 0.15$ . As in the  $q = 0.5$  case, for the frequency-locked solution, the two populations have nonzero within-population synchrony and intra-/interpopulation coupling strengths. However, the within-population synchrony and the intrapopulation coupling strength are no longer equal ( $\rho_1 \neq \rho_2$ ,  $\hat{\kappa}_{11} \neq \hat{\kappa}_{22}$ ). We note that the trivial solution ( $\rho_\mu = 0$ ,  $\hat{\kappa}_{\mu\nu} = 0$ ), which is stable for all values of  $\Delta\Omega$ , is not shown in Figure 9B, as it would have obscured the unstable region of the decoupled solution.

Finally, we performed a two-parameter continuation in  $\Delta\Omega$  and  $q$  (see Figure 9C). The saddle-node curves, which demarcate the region of existence for the coupled solution, are shown in green. The coupled solution exists between the two green curves. The orange curve corresponds to the pitchfork bifurcation, where the frequency-locked solution branches off the decoupled solution. There is a global bifurcation at  $q = 0.2 = 2\Delta/\lambda$  and  $q = 0.8 = 8\Delta/\lambda$ , when the decoupled solution ceases to exist, and so there is no longer a pitchfork bifurcation. The torus bifurcation curve, where the decoupled solution changes stability, is plotted in blue. In the region between the torus bifurcation curve and the saddle-node bifurcation curve, the two populations have nontrivial dynamics. The interpopulation coupling is weak enough that the populations do not entrain. Hence, the mean phases precess at different rates, and as such, the phase difference oscillates in time. As a result, the coupling strengths oscillate as the populations move in- and out-of-phase with each other. Given that the coupling strengths and the synchrony are interdependent, the synchrony variables also oscillate in time.

## 5 Describing the Full Adaptive Network Using Coupled Populations Evolving according to Mean-Field Dynamics

---

In this section, we aim to approximate a network of Kuramoto oscillators (see equation 2.1) with adaptivity given by symmetric PDDP (see equation 1.3 with  $\varphi = 0$ ) using two coupled populations evolving according to the mean-field dynamics. As shown in section 2.2, the full adaptive network with symmetric PDDP is itself a good approximation of the full adaptive network with symmetric STDP. Here, we optimize parameters of the coupled mean-field equations to best approximate the full network.

**5.1 Optimizing the Parameters of the Two-Population Mean-Field to Approximate the Full Adaptive Network.** To approximate the full adaptive network, we consider the two-population mean-field model,

$$\begin{cases} \frac{dZ_\mu}{dt} = (-\Delta_\mu + i\Omega_\mu)Z_\mu + \frac{1}{2} \sum_{v=1}^2 q_v \hat{\kappa}_{\mu v} (Z_v - \bar{Z}_v Z_\mu^2), \\ \frac{d\hat{\kappa}_{\mu v}}{dt} = \epsilon_\mu \epsilon_v [\lambda_\mu \lambda_v \operatorname{Re}(Z_\mu \bar{Z}_v) - \hat{\kappa}_{\mu v}], \end{cases} \quad (5.1)$$

where  $\mu, v \in \{1, 2\}$  are population indices,  $Z_\mu$  is the order parameter of population  $\mu$ , and  $\hat{\kappa}_{\mu v}$  is the average weight from population  $v$  to population  $\mu$ . Synthetic data from the full adaptive network are generated by simulating a network of  $N = 100$  Kuramoto oscillators (see equation 2.1) with adaptivity given by symmetric PDDP (see equation 1.3 with  $\varphi = 0$ ). Further details on the generation of synthetic data, as well as descriptions of the test and training sets are in appendix B.

To describe the full adaptive network using the two-population mean-field approximation, equation 5.1, we optimize  $\epsilon_\mu$  and  $\lambda_\mu$  with  $\mu \in \{1, 2\}$ , as well as the proportion of oscillators allocated to the first population denoted by  $q_1$ . Note that adaptivity parameters within and between populations ( $\lambda_1, \lambda_2, \epsilon_1, \epsilon_2$ ) are not the same as adaptivity parameters between oscillators in the full network ( $\lambda$  and  $\epsilon$ ). The optimal proportion of oscillators to allocate to each population is also unclear; we therefore optimize the allocation of oscillators as follows. We sort oscillators by the average value of their mean outgoing coupling (i.e.,  $\sum_{k=1}^N \kappa_{kl}/N$ ) and allocate the first  $100 \times q_1\%$  to the first population and the rest to the second population ( $q_2 = 1 - q_1$ ). This results in populations of size  $N_1$  and  $N_2$ , and initial conditions for equation 5.1 can be obtained from the initial conditions used to simulate the full adaptive network. For each initial condition, the parameters  $\Omega_\mu$  and  $\Delta_\mu$  are obtained as the median frequency and half of the interquartile range of the frequency of oscillators in each population, respectively. The optimization is performed as a sweep over  $q_1 = \{0.1, 0.2, 0.3, \dots, 0.9\}$ , and for each value of  $q_1$ , 36 local optimizations over the remaining parameters are carried out. Each local optimization starts from a random set of parameters and consists of successive optimizations using patternsearch and fminsearch (MatlabR2021a) over all initial conditions in the training set.

The cost function minimized by the optimization is the average over initial conditions in the training set of

$$\begin{aligned} c = & w_\rho \sum_n [\rho_{\text{mod}}(t_n) - \rho_{\text{dat}}(t_n)]^2 + w_\psi \sum_n [\psi_{\text{mod}}(t_n) - \psi_{\text{dat}}(t_n)]^2 \\ & + w_{\hat{\kappa}} \sum_n [\hat{\kappa}_{\text{mod}}(t_n) - \hat{\kappa}_{\text{dat}}(t_n)]^2, \end{aligned}$$

where  $t_n$  are all the time points corresponding to the second half of the simulation (to limit the influence of transients),  $\rho$  is the modulus of the order



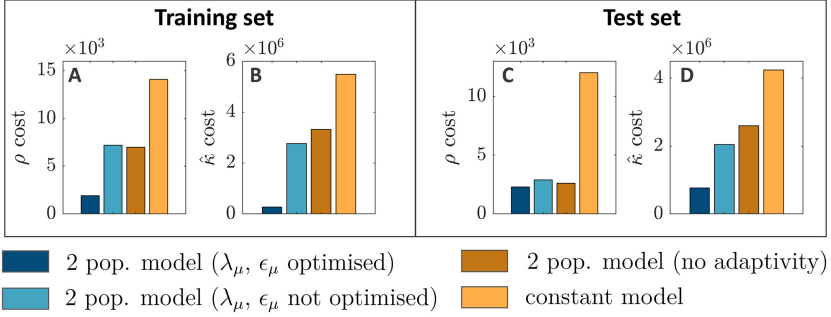


Figure 10: Performance of the two-population mean-field approximation. Each panel compares the sum of squared differences over time between model and synthetic data for  $\rho$  or  $\hat{k}$ , averaged over the training or test set. The two-population mean-field approximation with optimized plasticity parameters is shown in dark blue, the two-population mean-field approximation with plasticity parameters obtained from the full system is shown in light blue, the two-population model without adaptivity is shown in dark orange, and the constant model is shown in orange. Training and test sets are composed of 13 and 20 trajectories, respectively, with varied initial conditions (more details in appendix B).

parameter of the entire system,  $\psi$  is the (unwrapped) phase of the order parameter of the entire system,  $\hat{k}$  is the mean coupling weight of the entire system, and subscripts “mod” and “dat” refer to equation 5.1 and synthetic data from the full adaptive network, respectively. The coefficients  $w_\rho$ ,  $w_\psi$ ,  $w_{\hat{k}}$  are chosen to ensure that the costs corresponding to  $\rho$ ,  $\psi$ , and  $\hat{k}$  are on a similar scale. Compared to fitting only to the end point, our approach can capture nonconstant behaviors in  $\rho$  or  $\hat{k}$ , as well as frequency through phase evolution. For the two-population mean-field approximation, the order parameter of the whole system is obtained as  $Z = q_1 Z_1 + q_2 Z_2$ , and similarly the average coupling is obtained as  $\hat{k} = q_1^2 \hat{k}_{11} + q_2^2 \hat{k}_{22} + q_1 q_2 \hat{k}_{12} + q_1 q_2 \hat{k}_{21}$ .

**5.2 Performance on Training and Test Sets.** The optimized two-population mean-field approximation with the lowest cost was found for  $q_1 = 0.6$  (dark blue in Figure 10), and its parameters are given in Table 1. To test the model performance, we construct three control models; (1) a constant model defined from initial conditions by  $\rho = \rho_0$  and  $\hat{k} = \hat{k}_0$ , (2) a two-population mean-field approximation with  $q_1 = 0.6$  as in the fully optimized model but without adaptivity ( $\epsilon_1 = \epsilon_2 = 0$ ), and (3) a two-population mean-field approximation where  $\lambda_1 \lambda_2 = 25$  and  $\epsilon_1 \epsilon_2 = 0.5$  are chosen to match  $\lambda$  and  $\epsilon$ , respectively. For the third control model, we performed a sweep over  $q_1$  and found the best fit for  $q_1 = 0.95$ .

The fully optimized two-population mean-field approximation with the lowest cost on the training set is better at describing the dynamics of  $\rho$  and  $\hat{\kappa}$  on both the training set and the test set than the controls shown in Figure 10 in appendix C. This shows that to best reproduce synthetic data from the full adaptive model, it is necessary to consider both the evolution of the order parameter and of the average weights and to optimize the within- and between-population adaptivity parameters. The constant model is shown in light orange, the two-population mean-field approximation with no adaptivity is shown in dark orange, and the two-population mean-field approximation where the plasticity parameters are not optimized is in light blue. In the test set, the greatest improvement of the optimized two-population mean-field approximation over the controls is for  $\hat{\kappa}$  (Figure 10D). With the exception of the constant model, the controls already approximate  $\rho$  well in the test set, see Figure 10C. Representative trajectories of the two-population mean-field approximation obtained from initial conditions in the test set approximate the network synchrony, phase, and average coupling of synthetic data from the full adaptive network (see Figure 20 in appendix C). The approximation of  $\hat{\kappa}$  is overall better when  $\epsilon_\mu$  and  $\lambda_\mu$  are optimized. We note that while transients were not included in the cost function used to fit to synthetic data, they are relatively well described by the model when starting from random connectivity with different means in the test set (see Figure 20).

## 6 Discussion

---

Using simulations, we showed that PDDP and ebPDDP can provide useful approximations of STDP. In particular, single-harmonic rules can approximate simple forms of symmetric STDP, while multiharmonic rules are required to accurately approximate causal STDP. In the latter case, the accuracy of the approximation increases with the number of Fourier coefficients before reaching a plateau. The Fourier coefficients can be easily computed using analytical expressions only involving causal STDP parameters (see equation 2.6). We found ebPDDP to be a slightly better approximation than PDDP in the case of both symmetric STDP and causal STDP. This is expected since contrary to PDDP, ebPDDP restricts synaptic weight updates to spiking events, which is conceptually closer to STDP. One limitation of approximating STDP using plasticity rules based on phase difference is that the evolution of phase differences is required to be slower than the phase dynamics (Lübben et al., 2016). Under this assumption, the intricate evolution of coupling weights can be well approximated by PDDP and ebPDDP (see Figures 11 and 15 in appendix C). For best results, the STDP function should also decay to zero faster than the network mean frequency for both positive and negative spike-timing differences (in the case of causal STDP, to avoid both components in equation 2.3 strongly overlapping).

We derived exact expressions for the evolution of the average coupling weight in networks of phase oscillators with PDDP and ebPDDP. These expressions make no assumption about the underlying network (in particular, no assumption about the strength and type of coupling between oscillators), and are compatible with any plasticity rule based on phase difference as long as it can be expanded as a Fourier series of the phase difference. As a proof of principle, we focused on mean-field approximations based on the average coupling evolution for two-cluster states in a population of adaptive Kuramoto oscillators and performed a bifurcation analysis to highlight the different possible behaviors. Here we have focused predominantly on the Kuramoto model with adaptivity rules that mimic the adaptation between individual neural cells. However, as a prototypical model to study synchronization in neuroscience, the Kuramoto model has also found application on different scales including whole-brain modeling, epilepsy, and Parkinson's disease (Cumin & Unsworth, 2007; Breakspear et al., 2010; Cabral et al., 2014; Schmidt et al., 2015; Ponce-Alvarez et al., 2015; Finger et al., 2016; Asllani et al., 2018; Weerasinghe et al., 2019, 2021; Bick et al., 2020; Duchet et al., 2022). While here each Kuramoto oscillator typically represents neural populations rather than individual cells, our results may still help understand the role of adaptivity in such networks—albeit with potentially different adaptivity rules on different timescales.

Our framework could easily be adapted to consider more biologically realistic oscillator models, such as the  $\theta$ -neuron model or the formally equivalent quadratic integrate-and-fire (QIF) neuron model. Like the Kuramoto model, the  $\theta$ -neuron model is amenable to the Ott-Antonsen ansatz and as such, is amenable to exact mean-field description (Luke et al., 2013). For the QIF model, the equivalent Lorentzian ansatz should be used (Montbrió et al., 2015). The model analysis would be identical, but given the explicit phase dependency in the coupling, we can expect a richer set of dynamics for a network of  $\theta$ -neurons than observed here for Kuramoto oscillators. We could also include explicit synaptic variables, as in Byrne et al. (2020), to more accurately model synaptic processing. More generally, under the assumption of weak coupling, even more detailed neuron models, such as the Hodgkin-Huxley model, can be approximated by networks of phase oscillators through phase reduction (Brown et al., 2004; Pietras & Daffertshofer, 2019). While the resulting phase equations will generically contain higher-order terms that affect the global dynamics, a truncation to first order (i.e., Kuramoto-type coupling) can still provide suitable approximation where the first harmonics are dominant and shape the dynamics. While generic higher-order terms may break the Ott-Antonsen ansatz, its extensions (see, e.g., Vlasov et al., 2016; Tyulkina et al., 2018) or more general moment closure approaches (Kuehn, 2016) can provide suitable approximations that do not rely on a single order parameter to capture clustering; the dynamics of the mean coupling strength may then depend on more than a single order parameter. Indeed, previous studies of adaptive oscillators (Berner et al.,

2019) and our full network simulations point to the existence of three-, four-, and five-cluster states that motivate extending the results presented here. Although computationally expensive and, perhaps, numerically challenging, both the bifurcation analysis and model fitting could be extended to consider more than two clusters.

Combining theoretical insight and data-driven inference, we fitted a two-cluster mean-field approximation to a full adaptive network of Kuramoto oscillators in order to obtain a low-dimensional representation of the full system. The goal here is not to find a relationship between model parameters and (microscopic) parameters that could be measured in the brain (which is hardly ever possible with limited data), but to find a mean-field model with plasticity that can be used to describe population-level recordings, such as local field potentials. While the two-cluster mean-field model can approximate the full adaptive network on the test set, the accuracy of the approximation could be improved in several ways. First, a richer training set could be used. Second, the mean-field description of the order parameter is not exact, and a moment or cumulant approach may capture more of the full system dynamics (Tyulkina et al., 2018). Third, considering more than two populations may provide a more accurate approximation. Fourth, rather than allocating oscillators to clusters by thresholding their mean outgoing coupling, a finer partition could be learned (Snyder et al., 2020). Nevertheless, data-driven inference of low-dimensional representations of phase-oscillator networks (Thiem et al., 2020; Snyder et al., 2020; Fialkowski et al., 2022) is a promising approach to approximate the behavior of networks with STDP. Once clusters have been identified, a very recent mean-field technique based on the collective coordinate method can be used (Fialkowski et al., 2022).

More general types of STDP call for extensions of our framework. First, one would naturally expect that the strength of plastic connections is bounded. We included soft bounds in our investigation of symmetric STDP through a damping term (see equation 1.3), which is conserved in the average coupling (see equation 3.4), and is therefore present in the mean-field analyses carried out in sections 4 and 5. While neither soft nor hard bounds can easily be included in the average coupling derivation for causal STDP, we show that short transients of causal STDP with hard bounds are well captured by causal PDPD/ebPPD without bounds (see Figures 16 and 17 in appendix C). Second, we primarily focused on symmetric STDP rules, that is, interchanging the order of spikes will have little to no effect on the change of connection strength. For such adaptation, the network naturally forms clusters of strongly connected units (see Figure 3). By contrast, the causality of traditional asymmetric STDP rules will be reflected in the network structure as shown in Figure 5 and highlighted very recently in Thiele et al. (2023). To analyze the mean-field dynamics of such networks, a natural approach would be to computationally identify emerging feedforward structures in such networks instead of looking for clusters. In this case, finding a

corresponding low-dimensional description as in section 4 is more challenging. Third, we consider STDP adaptation rules that depend on pairs of oscillator states. More elaborate, spike-based rules such as triplet interactions have recently attracted attention (Pfister & Gerstner, 2006; Montangie et al., 2020). It would be interesting to have such adaptation reflected in the STDP model as these could be interpreted as “higher-order” network effects (see Bick et al., 2021).

As a step toward low-dimensional description of adaptive networks with STDP, our framework has implications for the study of long-term neural processes. In particular, the effects of clinically available DBS quickly disappear when stimulation is turned off; thus, stimulation needs to be provided continuously. To spare physiological activity as much as possible, it would therefore be highly desirable to design stimuli aimed at eliciting long-lasting effects. Continuous stimulation can also lead to habituation, where stimulation benefits diminish considerably over the years in some patients with essential tremor (Fasano & Helmich, 2019). Optimizing brain stimulation to have long-lasting effects so far has relied on computational studies (Tass & Majtanik, 2006; Popovych & Tass, 2012; Ebert et al., 2014; Popovych et al., 2015; Manos et al., 2018) or on analytical insights under the simplifying assumption that spiking is triggered only by stimulation pulses (Kromer & Tass, 2020). Other analytical approaches based on mean-field models are focused on short-term changes due to stimulation and do not consider plastic changes (Duchet et al., 2020; Weerasinghe et al., 2019, 2021). Our framework offers an alternative, where exact evolution equations for the average coupling within and between neural populations could inform the development of new therapies aimed at maximizing the long-term effects of brain stimulation. Although microscopic connectivity is unknown, stimulation can be designed to change average connectivity and impact synchrony as beneficial.

## Appendix A: Simulation Methods Used to Compare STDP to PDDP —

Using simulations, we compare networks of Kuramoto oscillators with adaptivity given by symmetric or causal STDP, to the same networks with adaptivity given by the corresponding single- or multiharmonic PDDP and ebPDDP rules.

**A.1 Symmetric Learning Rules.** We simulate networks of  $N = 60$  Kuramoto oscillators evolving according to equation 2.1, where the natural frequencies  $\omega_k$  are sampled from a normal distribution of mean  $\Omega = 10\pi$  (5 Hz) unless otherwise stated and standard deviation  $\Delta$ . A normal distribution was chosen over a Lorentzian distribution to avoid extreme natural frequencies, which lead to increased variability in simulation repeats. Initial conditions are also sampled from normal distributions. Phases  $\theta_k(t = 0 \text{ s})$  are sampled from the circular equivalent of  $\mathcal{N}(0, \pi^2/9)$  and couplings

$\kappa_{kl}(t = 0 \text{ s})$  from  $\mathcal{N}(5, \sigma_k^2)$ . The evolution of the coupling weights  $\kappa_{kl}$  is simulated according to equation 1.2 (symmetric STDP), together with the weight decay  $\frac{d\kappa_{kl}}{dt} = -\epsilon\kappa_{kl}$ , equation 1.3, with  $\varphi = 0$  (symmetric PDDP), or equation 2.2 (symmetric ebPDDP). For ebPDDP, we use  $\delta(t - t_k^q) \approx \mathbb{1}_{I_k^q}(t)/\Delta t$  where  $\mathbb{1}_{I_k^q}$  is the indicator function of  $I_k^q = [t_k^q, t_k^q + \Delta t)$  and  $\Delta t$  is the simulation time step. The network is simulated for 150 s, using the Euler method with  $\Delta t = 1 \text{ ms}$  unless otherwise stated. We use  $\epsilon = 0.5$ , and the values of other parameters are detailed in Figures 3 and 11.

**A.2 Causal Learning Rules.** Error metrics (described below) are computed between multiharmonic PDDP or ebPDDP and causal STDP for selected regions of parameter space. To limit computational cost, we constrain causal STDP parameters based on data and biological motivations. We use  $\tau_+ = 16.8 \text{ ms}$  and  $\tau_- = 33.7 \text{ ms}$ , which were obtained by fitting equation 1.1 to experimental data (data published in Bi & Poo, 1998, and fit in Bi & Poo, 2001). Several experimental studies have reported the LTD time constant  $\tau_-$  to be larger than the LTP time constant  $\tau_+$ , for example, in the rat hippocampus (Bi & Poo, 1998), somatosensory cortex (Feldman, 2000), and visual cortex (Froemke & Dan, 2002). We take  $A_+ = 0.2$  and  $A_-/A_+ = \beta$ . Since the time window for LTD is twice as long as the time window for LTP, we choose  $\beta = 0.5$  to study a balanced situation where LTP dominates for shorter spike-timing differences and LTD dominates for longer spike-timing differences, and  $\beta = 1$  to study a situation where LTD always dominates.

We simulate networks of Kuramoto oscillators as for symmetric STDP (see section A.2) with the following differences. Initial couplings  $\kappa_{kl}(t = 0 \text{ s})$  are sampled from  $\mathcal{N}(12, \sigma_k^2)$ . The evolution of the coupling weights  $\kappa_{kl}$  is simulated according to equation 1.1 (causal STDP), equation 2.3 (causal PDDP), or equation 2.4 (causal ebPDDP). For PDDP and ebPDDP, the Fourier expansion of  $F$  is truncated after  $N_f$  coefficients. No weight decay term is included.

The comparison of multiharmonic PDDP or ebPDDP to causal STDP relies on four error metrics. In the following error metric definitions, we use the subscript or superscript  $X$  to refer to quantities corresponding to multiharmonic PDDP or ebPDDP. To compare the time evolution of network synchrony, we define

$$e_\rho = \left\langle [\rho_X(t) - \rho_{\text{STDP}}(t)]^2 \right\rangle, \quad (\text{A.1})$$

where  $\langle \cdot \rangle$  denotes time averaging over the duration of the simulation  $[0, t_{\text{max}}]$  and  $\rho(t) = |Z(t)|$  is the network synchrony. To compare the time evolution of the network average coupling, we compute

$$e_{\hat{\kappa}} = \left\langle [\hat{\kappa}_x(t) - \hat{\kappa}_{\text{STDP}}(t)]^2 \right\rangle, \quad (\text{A.2})$$

where the average coupling is given by equation 3.1. The time evolution of the weight distribution is compared using

$$e_{\text{hist}(\kappa_{kl})} = \frac{n_{\text{bins}}^2}{N^4} \left\langle \sum_{j=1}^{n_{\text{bins}}} [h_j^x(t) - h_j^{\text{STDP}}(t)]^2 \right\rangle, \quad (\text{A.3})$$

where  $h_j(t)$  is the count of couplings weights falling into the  $j$ th bin in the histogram of coupling weights at time  $t$  (bin boundaries are identical across rules and time for a given set of parameters). The fourth error metric  $r_{\kappa_{kl}^\infty}$  is the Pearson's correlation coefficient between the STDP coupling matrix and the PDDP/ebPDDP coupling matrix at the last stimulation time point. The scaling factors in equation A.3 and the choice of a correlation measure for the fourth metric ensure that the corresponding metrics are independent of the size of the network and the number of bins. For each set of parameters, the four metrics are averaged across five repeats. For a given repeat and a given set of parameters, the same random samples are used as initial conditions to compare the network evolution between plasticity rules.

## Appendix B: Methodological Details Pertaining to the Optimization of the Two-Population Mean-Field Approximation

Synthetic data are generated by stimulating  $N = 100$  Kuramoto oscillators evolving according to equation 2.1, with adaptivity given by symmetric PDDP (equation 1.3 with  $\varphi = 0$ ,  $\lambda = 25$ , and  $\epsilon = 0.5$ ). Oscillator natural frequencies  $\omega_k$  are sampled from a Lorentzian distribution of center  $\Omega = 10\pi$  (5 Hz) and width  $\Delta = 0.6\pi$ . Initial phases are sampled from a Von Mises distribution of standard deviation  $\pi/4$ . Initial couplings  $\kappa_{kl}(t = 0 \text{ s})$  are sampled from  $\mathcal{N}(\hat{\kappa}_0, 0.5^2)$ . The network is simulated for 20 s, using the Euler method with  $\Delta t = 0.1 \text{ ms}$ .

We create a training set and a test set based on different initial conditions and in particular various  $\hat{\kappa}_0$ . The training set corresponds to  $\hat{\kappa}_0 = \{2, 2, 2, 3, 4, 5, 5, 10, 10, 15, 15, 15, 20\}$  and the test set to  $\hat{\kappa}_0 = \{3.5, 3.5, 3.5, 3.5, 7, 7, 7, 7, 12, 12, 12, 12, 17, 17, 17, 17, 22, 22, 22, 22\}$ . For each trajectory in the training and test sets, natural frequencies, initial phases, and initial couplings are sampled from their respective distributions. Repeated  $\hat{\kappa}_0$  values therefore correspond to different systems with different initial synchrony.

For optimization speed and accuracy, the two-population mean-field approximation is simulated using the variable order solver ode113 in Matlab (variable-step, variable-order Adams-Bashforth-Moulton solver of orders 1 to 13).



## Appendix C: Supplementary Figures and Tables

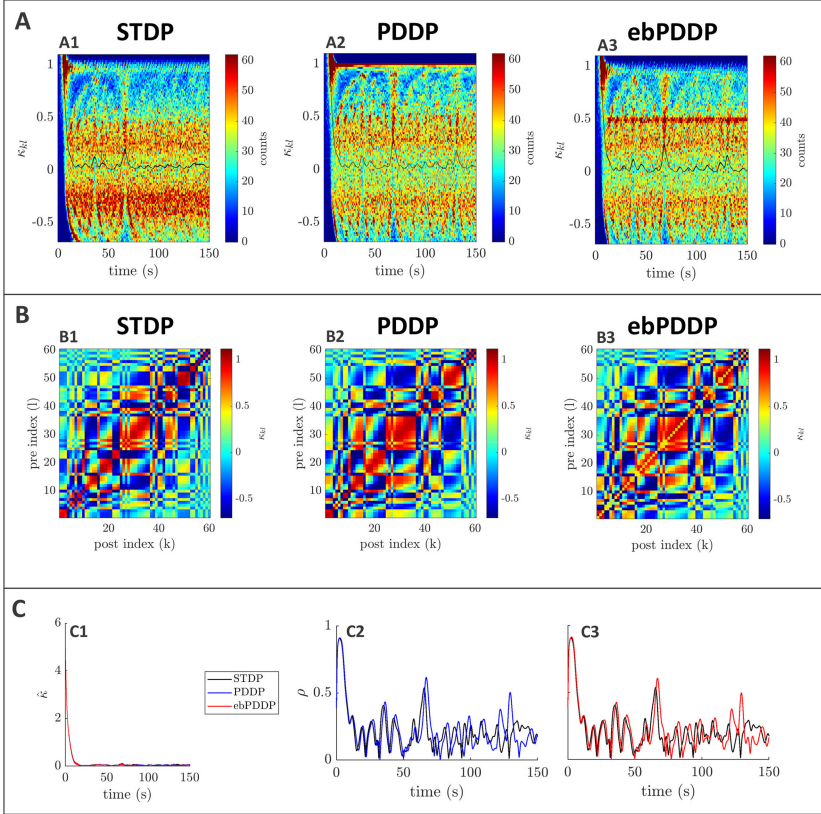


Figure 11: Comparison between symmetric STDP and PDDP in a Kuramoto network (desynchronized state). (A) Evolution of the distribution of coupling weights with time (100 bins at each time point). The average weight is represented by a thin black line. STDP is shown in panel A1, PDDP in panel A2, and ebPDDP in panel A3. (B) Coupling matrix at  $t = 150$  s, with oscillators sorted by natural frequency. STDP is shown in panel B1, PDDP in panel B2, and ebPDDP in panel B3. (C) Time evolution of average coupling (panel C1: error bars represent the standard error of the mean over five repeats, too small to see) and network synchrony (C2 and C3). STDP is shown in black, PDDP in blue, and ebPDDP in red.  $a = 0.025822$ ,  $b = 0.049415$ ,  $\sigma_K = 3$ ,  $\Delta = 0.2\pi$ ,  $\Omega = 10\pi$  (5 Hz).



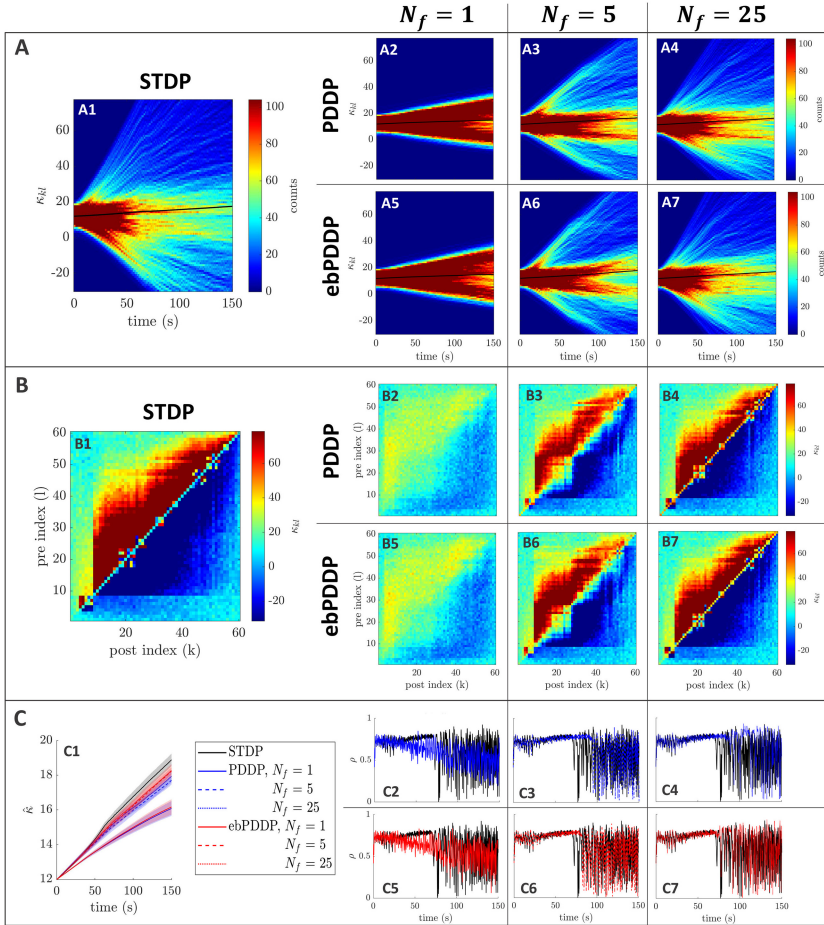


Figure 12: Comparison between STDP and PDDP in a Kuramoto network,  $[\beta = 0.5, \sigma_\kappa = 3, \Delta = 1.8\pi, \Omega = 10\pi$  (5 Hz)]. Results for PDDP and ebPDDP are shown for 1, 5, and 25 Fourier components  $N_f$  (first, second, and third columns on the right hand-side of the figure, respectively). (A) Evolution of the distribution of coupling weights with time (100 bins at each time point). The average weight is represented by a thin black line. STDP is shown in panel A1, PDDP in panels A2 to A4, and ebPDDP in panels A5 to A7. (B) Coupling matrix at  $t = 150$  s, with oscillators sorted by natural frequency. STDP is shown in panel B1, PDDP in panels B2 to B4, and ebPDDP in panels B5 to B7. (C) Time evolution of average coupling (panel C1: error bars represent the standard error of the mean over five repeats) and network synchrony (panels C2 to C7). STDP is shown in black, PDDP in blue, and ebPDDP in red.

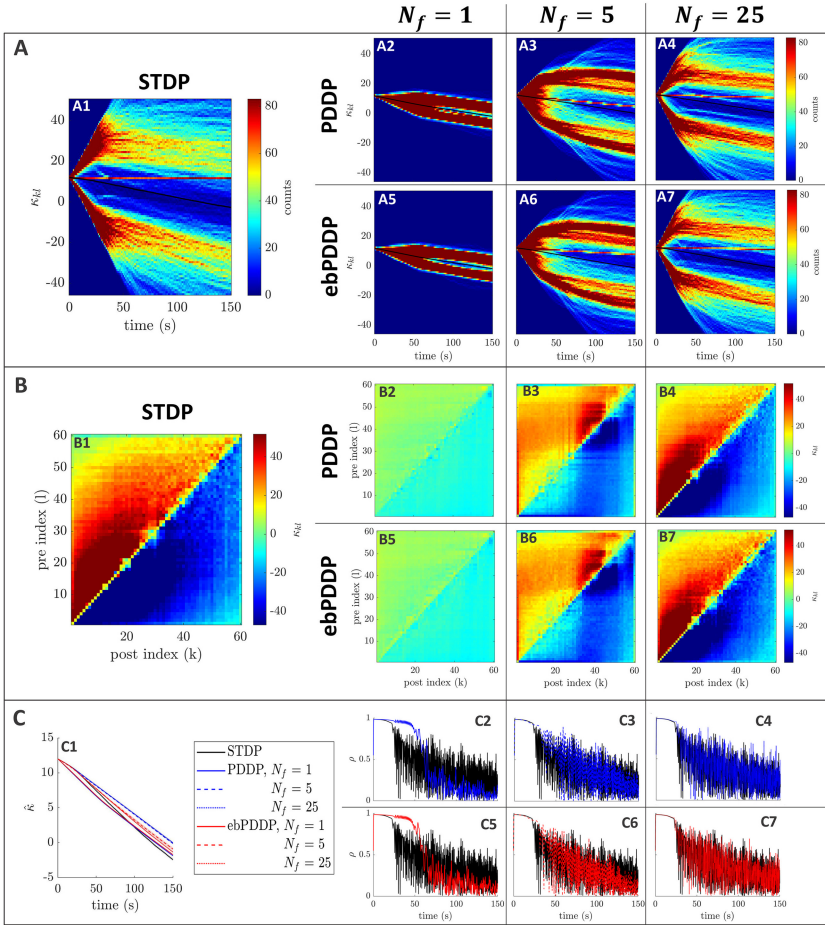


Figure 13: Comparison between STDP and PDDP in a Kuramoto network,  $[\beta = 1, \sigma_k = 0.2, \Delta = 0.6\pi, \Omega = 10\pi$  (5 Hz)]. Results for PDDP and ebPDDP are shown for 1, 5, and 25 Fourier components  $N_f$  (first, second, and third columns on the right-hand side of the figure, respectively). (A) Evolution of the distribution of coupling weights with time (100 bins at each time point). The average weight is represented by a thin black line. STDP is shown in panel A1, PDDP in panels A2 to A4, and ebPDDP in panels A5 to A7. (B) Coupling matrix at  $t = 150$  s, with oscillators sorted by natural frequency. STDP is shown in panel B1, PDDP in panels B2 to B4, and ebPDDP in panels B5 to B7. (C) Time evolution of average coupling (panel C1: error bars represent the standard error of the mean over five repeats) and network synchrony (panels C2 to C7). STDP is shown in black, PDDP in blue, and ebPDDP in red.

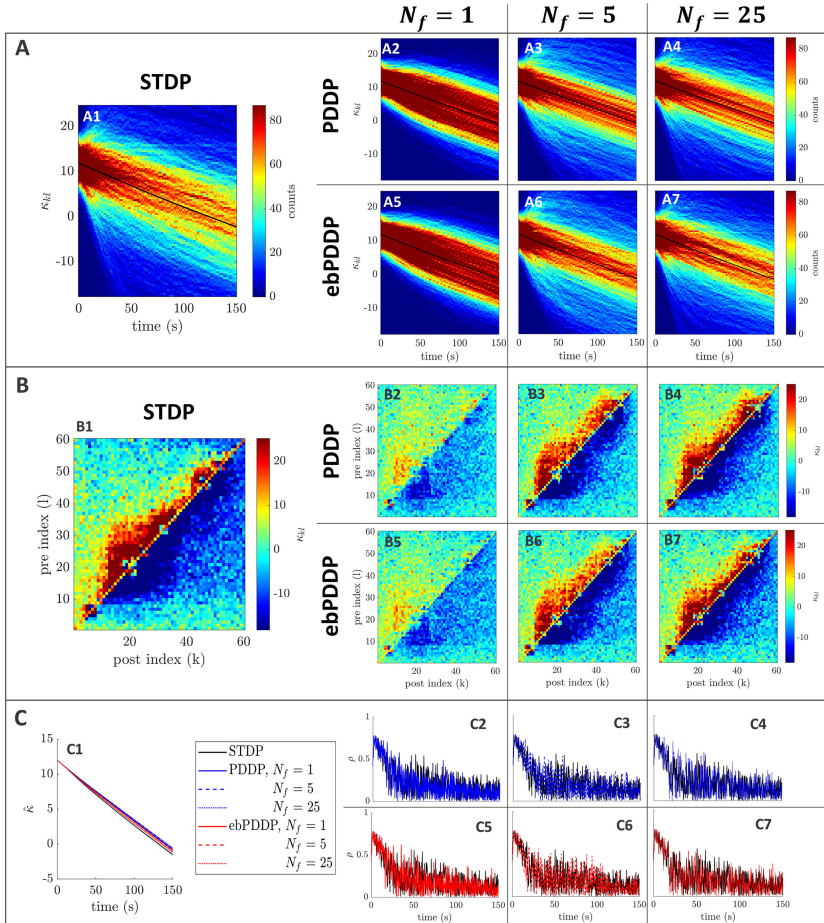


Figure 14: Comparison between STDP and PDDP in a Kuramoto network,  $[\beta = 1, \sigma_\kappa = 3, \Delta = 1.8\pi, \Omega = 10\pi$  (5 Hz)]. Results for PDDP and ebPDDP are shown for 1, 5, and 25 Fourier components  $N_f$  (first, second, and third columns on the right-hand side of the figure, respectively). (A) Evolution of the distribution of coupling weights with time (100 bins at each time point). The average weight is represented by a thin black line. STDP is shown in panel A1, PDDP in panels A2 to A4, and ebPDDP in panel A5 to A7. (B) Coupling matrix at  $t = 150$  s, with oscillators sorted by natural frequency. STDP is shown in panel B1, PDDP in panels B2 to B4, and ebPDDP in panels B5 to B7. (C) Time evolution of average coupling (panel C1: error bars represent the standard error of the mean over five repeats) and network synchrony (panels C2 to C7). STDP is shown in black, PDDP in blue, and ebPDDP in red.

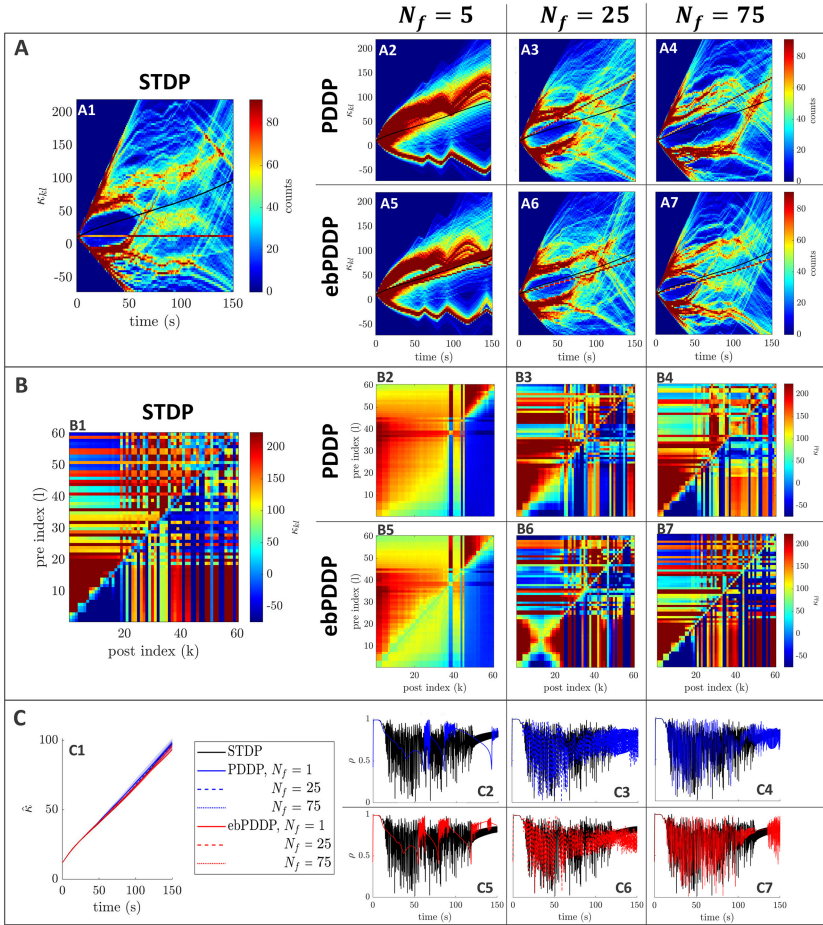


Figure 15: Comparison between STDP and PDDP in a Kuramoto network,  $[\beta = 0.5, \sigma_\kappa = 0.2, \Delta = 0.6\pi, \Omega = 40\pi$  (20 Hz),  $\Delta t = 0.1$  ms]. Results for PDDP and ebPDDP are shown for 5, 25, and 75 Fourier components  $N_f$  (first, second, and third columns on the right-hand side of the figure, respectively). (A) Evolution of the distribution of coupling weights with time (100 bins at each time point). The average weight is represented by a thin black line. STDP is shown in panel A1, PDDP in panels A2 to A4, and ebPDDP in panels A5 to A7. (B) Coupling matrix at  $t = 150$  s, with oscillators sorted by natural frequency. STDP is shown in panel B1, PDDP in panels B2 to B4, and ebPDDP in panels B5 to B7. (C) Time evolution of average coupling (panel C1: error bars represent the standard error of the mean over five repeats) and network synchrony (panels C2 to C7). STDP is shown in black, PDDP in blue, and ebPDDP in red.

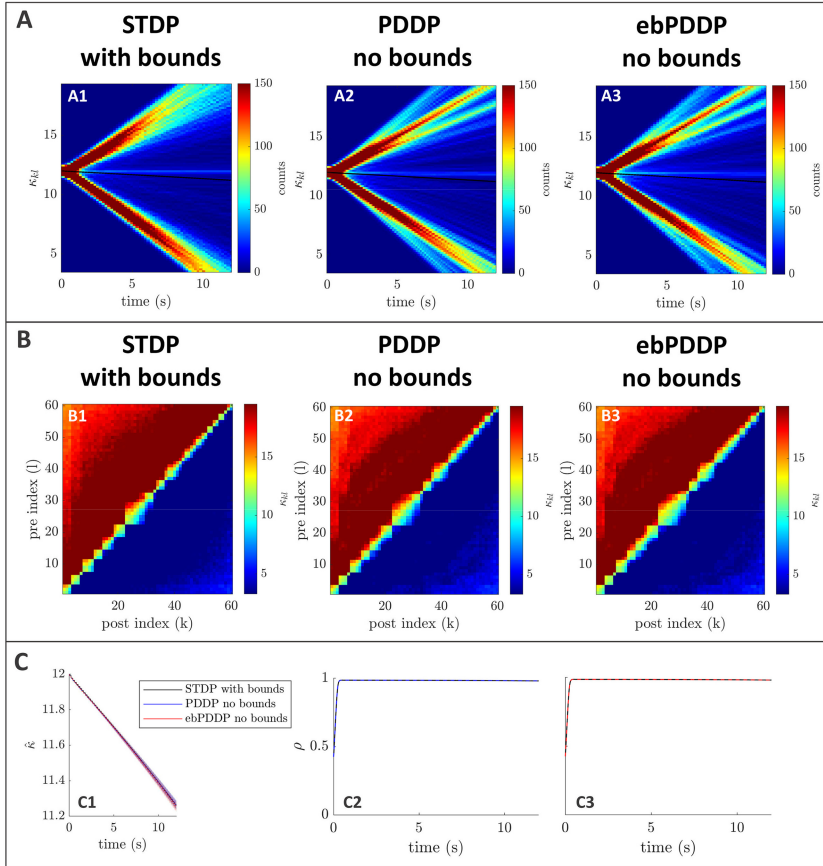


Figure 16: Comparison between STDP with hard bounds and PDDP without bounds in a Kuramoto network,  $[\beta = 1, \sigma_\kappa = 0.2, \Delta = 0.6\pi, \Omega = 10\pi$  (5 Hz)]. Results for PDDP and ebPDDP are shown for  $N_f = 40$  Fourier components. For STDP, hard bounds are enforced such that no individual weight can go below 0 or above 30. (A) Evolution of the distribution of coupling weights with time (100 bins at each time point). The average weight is represented by a thin black line. STDP with hard bounds is shown in panel A1, PDDP without bounds in panel A2, and ebPDDP without bounds in panel A3. (B) Coupling matrix at  $t = 12$  s, with oscillators sorted by natural frequency. STDP with hard bounds is shown in panel B1, PDDP without bounds in panel B2, and ebPDDP without bounds in panel B3. (C) Time evolution of average coupling (panel C1: error bars represent the standard error of the mean over five repeats) and network synchrony (panels C2 and C3). STDP with hard bounds is shown in black, PDDP without bounds in blue, and ebPDDP without bounds in red.



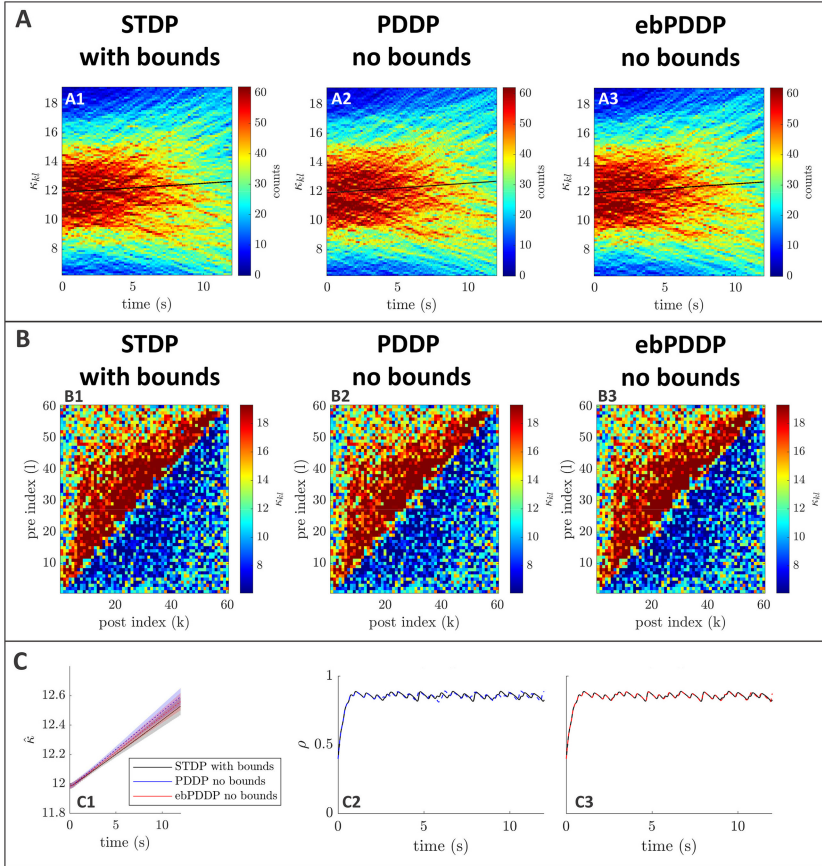


Figure 17: Comparison between STDP with hard bounds and PDDP without bounds in a Kuramoto network,  $[\beta = 0.5, \sigma_\kappa = 3, \Delta = 1.8\pi, \Omega = 10\pi$  (5 Hz)]. Results for PDDP and ebPDDP are shown for  $N_f = 40$  Fourier components. For STDP, hard bounds are enforced such that no individual weight can go below 0 or above 30. (A) Evolution of the distribution of coupling weights with time (100 bins at each time point). The average weight is represented by a thin black line. STDP with hard bounds is shown in panel A1, PDDP without bounds in panel A2, and ebPDDP without bounds in panel A3. (B) Coupling matrix at  $t = 12$  s, with oscillators sorted by natural frequency. STDP with hard bounds is shown in panel B1, PDDP without bounds in panel B2, and ebPDDP without bounds in panel B3. (C) Time evolution of average coupling (panel C1: error bars represent the standard error of the mean over five repeats) and network synchrony (panels C2 and C3). STDP with hard bounds is shown in black, PDDP without bounds in blue, and ebPDDP without bounds in red.

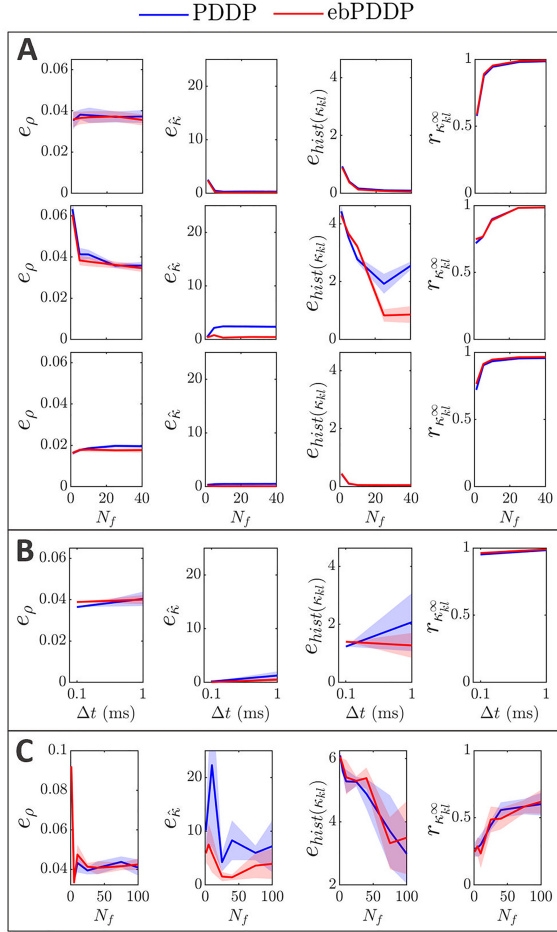


Figure 18: Influence of  $N_f$ ,  $\Delta t$ , and network frequency on error metrics. Error metrics for PDDP compared to STDP for the time evolution of network synchrony  $e_\rho$ , average coupling  $e_{\hat{\kappa}}$  and distribution of weights  $e_{\text{hist}(\kappa_{kl})}$ , and for the coupling matrix at the last stimulation point  $\tau_{\kappa_{kl}}^\infty$  are shown in the first, second, third, and fourth columns, respectively. Results for PDDP are in blue and for ebPDDP in red. Showing SEM error bars over five repeats. (A) Influence of the number of Fourier coefficients  $N_f$  on the error metrics for the parameters used in Figure 12 ( $\beta = 0.5$ ,  $\sigma_\kappa = 3$ ,  $\Delta = 1.8\pi$ ,  $\Omega = 10\pi$ ) in the first row; in Figure 13 ( $\beta = 1$ ,  $\sigma_\kappa = 0.2$ ,  $\Delta = 0.6\pi$ ,  $\Omega = 10\pi$ ) in the second row; and in Figure 14 ( $\beta = 1$ ,  $\sigma_\kappa = 3$ ,  $\Delta = 1.8\pi$ ,  $\Omega = 10\pi$ ) in the third row. (B) Influence of the time step  $\Delta t$  for the parameters used in Figure 5 ( $\beta = 0.5$ ,  $\sigma_\kappa = 0.2$ ,  $\Delta = 0.6\pi$ ,  $\Omega = 10\pi$ ) and  $N_f = 40$ . (C) Influence of the number of Fourier coefficients  $N_f$  on error metrics for the parameters used in the 20 Hz example, see Figure 15 ( $\beta = 0.5$ ,  $\sigma_\kappa = 0.2$ ,  $\Delta = 0.6\pi$ ,  $\Omega = 40\pi$ ,  $\Delta t = 0.1$  ms).

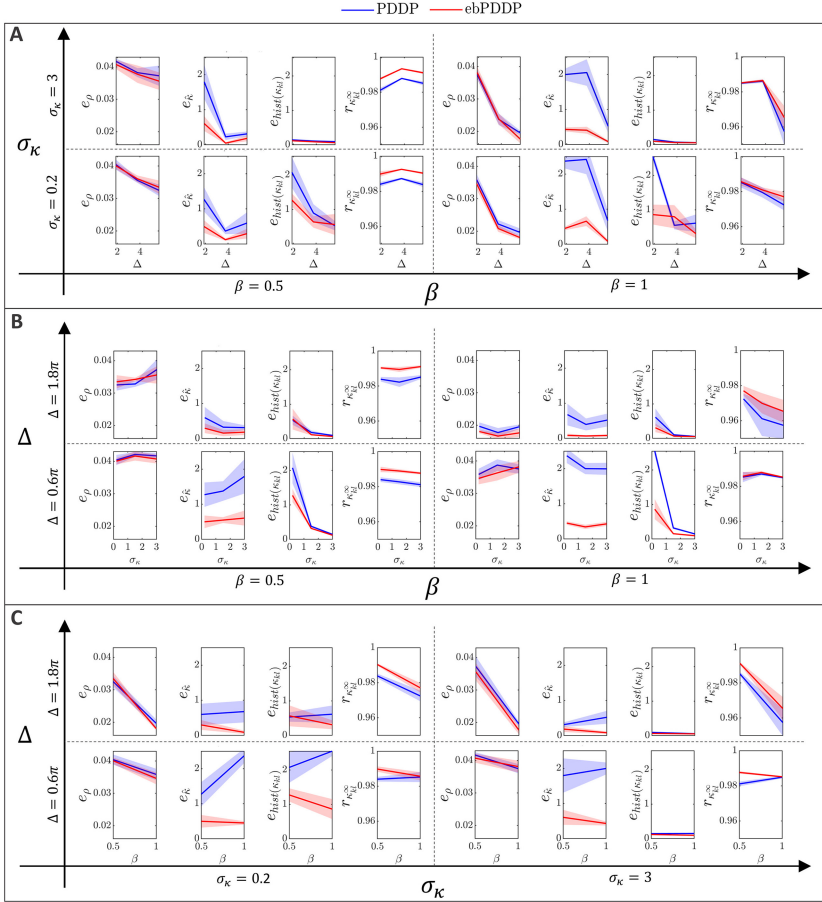


Figure 19: Influence of  $\sigma_\kappa$ ,  $\Delta$ , and  $\beta$  on error metrics (slices through parameter space). Error metrics for PDDP compared to STDP for the time evolution of network synchrony  $e_p$  (first and fifth columns), average coupling  $e_k$  (second and sixth columns), and distribution of weights  $e_{\text{hist}(k_{kl})}$  (third and seventh columns), and for the coupling matrix at the last stimulation point  $r_{k_{kl}}^\infty$  (fourth and eighth columns). Results for PDDP are in blue and for ebPDDP in red. Each of the panels represents a different slice through parameter space as indicated by the axes. The error metrics are shown for  $N_f = 40$  Fourier components, with sem error bars over five repeats.



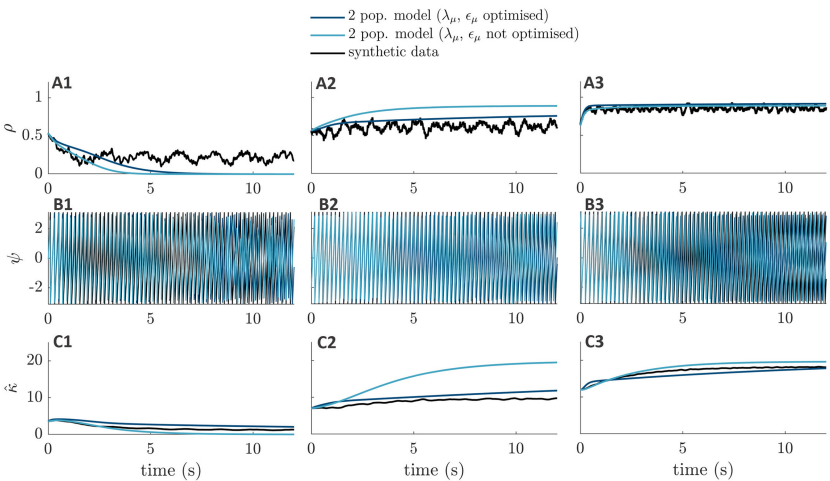


Figure 20: Representative trajectories from initial conditions in the test set. The two-population mean-field approximation with optimized plasticity parameters is shown in dark blue, the two-population mean-field approximation with plasticity parameters obtained from the full system is shown in light blue, and synthetic data from the full adaptive Kuramoto network are shown in black. The first row shows the network synchrony, the second row the network phase, and the third row the network average coupling.

Table 1: Best Parameters of Two-Population Mean-Field Approximation.

Parameter	$\epsilon_1$	$\epsilon_2$	$\lambda_1$	$\lambda_2$
Value	0.0263	3.0262	5.2985	5.4759

Notes: Parameters correspond to equation 5.1. Full network parameters used to generate synthetic data for the optimization are given in appendix B.

Acknowledgments

We are grateful to Rafal Bogacz and Alessandro Torcini for helpful discussions. We acknowledge the use of the University of Oxford Advanced Research Computing facility in carrying out this work <http://dx.doi.org/10.5281/zenodo.22558>

Funding Information

B.D. was supported by Medical Research Council grant MC\_UU\_00003/1. C.B. acknowledges support from the Engineering and Physical Sciences Research Council through grant EP/T013613/1.

## Data Availability Statement

---

No new data were created or analyzed in this study. We are sharing code at <https://github.com/benoit-du/STDPvsPDDP> to compare the evolution of a Kuramoto network with STDP to the evolution of a Kuramoto network with PDDP and ebPDDP.

## References

---

- Abbott, L. F., & Nelson, S. B. (2000). Synaptic plasticity: Taming the beast. *Nature Neuroscience*, 3(11), 1178–1183. 10.1038/81453, PubMed: 11127835
- Adamchic, I., Hauptmann, C., Barnikol, U. B., Pawelczyk, N., Popovych, O., Barnikol, T. T., . . . Tass, P. A. (2014). Coordinated reset neuromodulation for Parkinson's disease: Proof-of-concept study. *Movement Disorders*, 2(13), 1679–1684. 10.1002/mds.25923
- Akil, A. E., Rosenbaum, R., & Josić, K. (2021). Balanced networks under spike-time dependent plasticity. *PLOS Computational Biology* 17(5), e1008958. 10.1371/journal.pcbi.1008958
- Aoki, T., & Aoyagi, T. (2009). Co-evolution of phases and connection strengths in a network of phase oscillators. *Physical Review Letters* 102(3). 10.1103/PhysRevLett.102.034101
- Ashwin, P., Coombes, S., & Nicks, R. (2016). Mathematical frameworks for oscillatory network dynamics in neuroscience. *Journal of Mathematical Neuroscience* 6(1), 2. 10.1186/s13408-015-0033-6
- Aslani, M., Expert, P., & Carletti, T. (2018). A minimally invasive neurostimulation method for controlling abnormal synchronisation in the neuronal activity. *PLOS Computational Biology*, 14(7), e1006296. 10.1371/journal.pcbi.1006296
- Berner, R., Schöll, E., & Yanchuk, S. (2019). Multiclusters in networks of adaptively coupled phase oscillators. *SIAM Journal on Applied Dynamical Systems*, 18(4), 2227–2266. 10.1137/18M1210150
- Bi, G. Q., & Poo, M. M. (1998). Synaptic modifications in cultured hippocampal neurons: Dependence on spike timing, synaptic strength, and postsynaptic cell type. *Journal of Neuroscience*, 18(24), 10464–10472. 10.1523/jneurosci.18-24-10464.1998, PubMed: 9852584
- Bi, G. Q., & Poo, M. M. (2001). Synaptic modification by correlated activity: Hebb's postulate revisited. *Annual Review of Neuroscience* 24, 139–166. 10.1146/annurev.neuro.24.1.139, PubMed: 11283308
- Bick, C., Goodfellow, M., Laing, C. R., & Martens, E. A. (2020). Understanding the dynamics of biological and neural oscillator networks through exact mean-field reductions: A review. *Journal of Mathematical Neuroscience*, 10(1), 10. 10.1186/s13408-020-00086-9
- Bick, C., Gross, E., Harrington, H. A., & Schaub, M. T. (2021). *What are higher-order networks?* arXiv:2104.11329.
- Breakspear, M., Heitmann, S., & Daffertshofer, A. (2010). Generative models of cortical oscillations: Neurobiological implications of the Kuramoto model. *Frontiers in Human Neuroscience*, 4, 190. 10.3389/fnhum.2010.00190

- Brown, E., Moehlis, J., & Holmes, P. (2004). On the phase reduction and response dynamics of neural oscillator populations. *Neural Computation*, 16, 673–715. 10.1162/089976604322860668
- Byrne, Á., O'Dea, R. D., Forrester, M., Ross, J., & Coombes, S. (2020). Next-generation neural mass and field modeling. *Journal of Neurophysiology*, 123(2), 726–742. 10.1152/jn.00406.2019, PubMed: 31774370
- Cabral, J., Luckhoo, H., Woolrich, M., Joensson, M., Mohseni, H., Baker, A., . . . Deco, G. (2014). Exploring mechanisms of spontaneous functional connectivity in MEG: How delayed network interactions lead to structured amplitude envelopes of band-pass filtered oscillations. *NeuroImage*, 90, 423–435. 10.1016/j.neuroimage.2013.11.047, PubMed: 24321555
- Cassenaer, S., & Laurent, G. (2007). Hebbian STDP in mushroom bodies facilitates the synchronous flow of olfactory information in locusts. *Nature*, 448(7154), 709–713. 10.1038/nature05973, PubMed: 17581587
- Ciszak, M., Marino, F., Torcini, A., & Olmi, S. (2020). Emergent excitability in populations of nonexcitable units. *Physical Review E*, 102(5), 050201. 10.1103/PhysRevE.102.050201
- Coombes, S., & Byrne, Á. (2019). Next generation neural mass models. In F. Corinto & A. Torcini (Eds.), *Nonlinear dynamics in computational neuroscience* (pp. 1–16). Springer. 10.1007/978-3-319-71048-8\_1
- Coulon, A., Beslon, G., & Soula, H. A. (2011). Enhanced stimulus encoding capabilities with spectral selectivity in inhibitory circuits by STDP. *Neural Computation*, 23(4), 882–908. 10.1162/NECO\_a\_00100, PubMed: 21222530
- Cumin, D., & Unsworth, C. (2007). Generalising the Kuramoto model for the study of neuronal synchronisation in the brain. *Physica D: Nonlinear Phenomena*, 226(2), 181–196. 10.1016/j.physd.2006.12.004
- Duchet, B., Sermon, J. J., Weerasinghe, G., Denison, T., & Bogacz, R. (2022). *How to entrain a selected neuronal rhythm but not others: Open-loop dithered brain stimulation for selective entrainment*. bioRxiv:2022.07.06.499051. 10.1101/2022.07.06.499051
- Duchet, B., Weerasinghe, G., Cagnan, H., Brown, P., Bick, C., & Bogacz, R. (2020). Phase-dependence of response curves to deep brain stimulation and their relationship: From essential tremor patient data to a Wilson–Cowan model. *Journal of Mathematical Neuroscience*, 10(1), 10. 10.1186/s13408-020-00081-0
- Ebert, M., Hauptmann, C., & Tass, P. A. (2014). Coordinated reset stimulation in a large-scale model of the STN-GPE circuit. *Frontiers in Computational Neuroscience*, 8, 154. 10.3389/fncom.2014.00154
- Ermentrout, B. (2002). *Simulating, analyzing, and animating dynamical systems*. Society for Industrial and Applied Mathematics. 10.1137/1.9780898718195
- Fasano, A., & Helmich, R. C. (2019). Tremor habituation to deep brain stimulation: Underlying mechanisms and solutions. *Movement Disorders*, 34(12), 1761–1773. 10.1002/mds.27821, PubMed: 31433906
- Feldman, D. E. (2000). Timing-based LTP and LTD at vertical inputs to layer II/III pyramidal cells in rat barrel cortex. *Neuron*, 27(1), 45–56. 10.1016/S0896-6273(00)00008-8, PubMed: 10939330
- Fialkowski, J., Yanchuk, S., Sokolov, I. M., Schöll, E., Gottwald, G. A., & Berner, R. (2022). *Heterogeneous nucleation in finite size adaptive dynamical networks*. arXiv:2207.02939.

- Finger, H., Bönstrup, M., Cheng, B., Messé, A., Hilgetag, C., Thomalla, G., . . . König, P. (2016). Modeling of large-scale functional brain networks based on structural connectivity from DTI: Comparison with EEG derived phase coupling networks and evaluation of alternative methods along the modeling Path. *PLOS Computational Biology*, 12(8), e1005025. 10.1371/journal.pcbi.1005025
- Froemke, R. C., & Dan, Y. (2002). Spike-timing-dependent synaptic modification induced by natural spike trains. *Nature*, 416(6879), 433–438. 10.1038/416433a, PubMed: 11919633
- Gast, R., Knöschke, T. R., & Schmidt, H. (2021). Mean-field approximations of networks of spiking neurons with short-term synaptic plasticity. *Physical Review E*, 10, 44310. 10.1103/physreve.104.044310
- Gast, R., Schmidt, H., & Knöschke, T. R. (2020). A mean-field description of bursting dynamics in spiking neural networks with short-term adaptation. *Neural Computation*, 32(9), 1615–1634. 10.1162/neco\_a\_01300, PubMed: 32687770
- Gerstner, W., Kempter, R., Van Hemmen, J. L., & Wagner, H. (1996). A neuronal learning rule for sub-millisecond temporal coding. *Nature*, 383(6595), 76–78. 10.1038/383076a0, PubMed: 8779718
- Gkogkas, M. A., Kuehn, C., & Xu, C. (2021). *Continuum limits for adaptive network dynamics*. arXiv:2109.05898.
- Hebb, D. (2005). *The organization of behavior: A neuropsychological theory*. Psychology Press. 10.4324/9781410612403
- Johnen, V. M., Neubert, F. X., Buch, E. R., Verhagen, L. M., O'Reilly, J., Mars, R. B., & Rushworth, M. F. (2015). Causal manipulation of functional connectivity in a specific neural pathway during behaviour and at rest. *eLife*, 2015(4). 10.7554/eLife.04585
- Kim, K., Yoo, S. J., Kim, S. Y., Lee, T., Lim, S. H., Jang, J. E., . . . Choi, J. W. (2021). Subthreshold electrical stimulation as a low power electrical treatment for stroke rehabilitation. *Scientific Reports*, 11(1), 11. 10.1038/s41598-021-93354-x
- Kromer, J. A., & Tass, P. A. (2020). Long-lasting desynchronization by decoupling stimulation. *Physical Review Research*, 2(3), 2. 10.1103/physrevresearch.2.033101
- Kuehn, C. (2016). Moment closure—A brief review. In E. Schöll, S. Klapp, & P. Hövel (Eds.), *Control of self-organizing nonlinear systems* (pp. 253–271). Springer. 10.1007/978-3-319-28028-8\_13
- Kuramoto, Y. (1975). Self-entrainment of a population of coupled non-linear oscillators. In *International Symposium on Mathematical Problems in Theoretical Physics* (pp. 420–422).
- Litwin-Kumar, A., & Doiron, B. (2014). Formation and maintenance of neuronal assemblies through synaptic plasticity. *Nature Communications*, 5(1), 1–12. 10.1038/ncomms6319
- Lücken, L., Popovych, O. V., Tass, P. A., & Yanchuk, S. (2016). Noise-enhanced coupling between two oscillators with long-term plasticity. *Physical Review E*, 93(3). 10.1103/PhysRevE.93.032210
- Luke, T. B., Barreto, E., & So, P. (2013). Complete classification of the macroscopic behaviour of a heterogeneous network of theta neurons. *Neural Computation*, 25, 3207–3234. 10.1162/NECO\_a\_00525
- Madadi Asl, M., Vahabie, A.-H., Valizadeh, A., & Tass, P. A. (2022, Mar). Spike-timing-dependent plasticity mediated by dopamine and its role in Parkinson's

- disease pathophysiology. *Frontiers in Network Physiology*, 10. 10.3389/FNETP.2022.817524
- Maistrenko, Y. L., Lysyansky, B., Hauptmann, C., Burylko, O., & Tass, P. A. (2007). Multistability in the Kuramoto model with synaptic plasticity. *Physical Review E—Statistical, Nonlinear, and Soft Matter Physics*, 75(6). 10.1103/PhysRevE.75.066207
- Manos, T., Zeitler, M., & Tass, P. A. (2018). How stimulation frequency and intensity impact on the long-lasting effects of coordinated reset stimulation. *PLOS Computational Biology*, 14(5). 10.1371/journal.pcbi.1006113
- Markram, H., Lübke, J., Frotscher, M., & Sakmann, B. (1997). Regulation of synaptic efficacy by coincidence of postsynaptic APs and EPSPs. *Science*, 275(5297), 213–215. 10.1126/science.275.5297.213, PubMed: 8985014
- Mishra, R. K., Kim, S., Guzman, S. J., & Jonas, P. (2016). Symmetric spike timing-dependent plasticity at CA3-CA3 synapses optimizes storage and recall in autoassociative networks. *Nature Communications*, 7. 10.1038/ncomms11552
- Montangie, L., Miehl, C., & Gjorgjieva, J. (2020). Autonomous emergence of connectivity assemblies via spike triplet interactions. *PLOS Computational Biology*, 16(5), e1007835. 10.1371/journal.pcbi.1007835
- Montbrió, E., Pazó, D., & Roxin, A. (2015). Macroscopic description for networks of spiking neurons. *Physical Review*, 10(5), 021028. 10.1103/PhysRevX.5.021028
- Müller-Dahlhaus, F., Ziemann, U., & Classen, J. (2010). Plasticity resembling spike-timing dependent synaptic plasticity: The evidence in human cortex. *Frontiers in Synaptic Neuroscience*, 2. 10.3389/fnsyn.2010.00034
- Nguyen, P. T. M., Hayashi, Y., Baptista, M. D. S., & Kondo, T. (2020). Collective almost synchronization-based model to extract and predict features of EEG signals. *Scientific Reports*, 10(1), 10. 10.1038/s41598-020-73346-z
- Ocker, G. K. Litwin-Kumar, A., & Doiron, B. (2015). Self-organization of microcircuits in networks of spiking neurons with plastic synapses. *PLOS Computational Biology*, 11(8), 11. 10.1371/journal.pcbi.1004458
- Ott, E., & Antonsen, T. M. (2008). Low dimensional behavior of large systems of globally coupled oscillators. *Chaos: An Interdisciplinary Journal of Nonlinear Science*, 18(3), 18. 10.1063/1.2930766
- Ott, E., & Antonsen, T. M. (2009). Long time evolution of phase oscillator systems. *Chaos*, 19(2), 19. 10.1063/1.3136851
- Pfister, J. P., & Gerstner, W. (2006). Triplets of spikes in a model of spike timing-dependent plasticity. *Journal of Neuroscience*, 26(38), 9673–9682. 10.1523/JNEUROSCI.1425-06.2006, PubMed: 16988038
- Pietras, B., & Daffertshofer, A. (2019). Network dynamics of coupled oscillators and phase reduction techniques. *Physics Reports*, 819, 1–105. 10.1016/j.physrep.2019.06.001
- Ponce-Alvarez, A., Deco, G., Hagmann, P., Romani, G. L., Mantini, D., & Corbetta, M. (2015). Resting-state temporal synchronization networks emerge from connectivity topology and heterogeneity. *PLOS Computational Biology*, 11(2), e1004100. 10.1371/journal.pcbi.1004100
- Popovych, O. V., & Tass, P. A. (2012). Desynchronizing electrical and sensory coordinated reset neuromodulation. *Frontiers in Human Neuroscience*, 6(2012), 1–14. 10.3389/fnhum.2012.00058, PubMed: 22279433

- Popovych, O. V., Xenakis, M. N., & Tass, P. A. (2015). The spacing principle for unlearning abnormal neuronal synchrony. *PLOS One*, 10(2), e0117205. 10.1371/journal.pone.0117205
- Röhr, V., Berner, R., Lameu, E. L., Popovych, O. V., & Yanchuk, S. (2019). Frequency cluster formation and slow oscillations in neural populations with plasticity. *PLOS One*, 14(11), e0225094. 10.1371/journal.pone.0225094
- Schmidt, R., LaFleur, K. J., de Reus, M. A., van den Berg, L. H., & van den Heuvel, M. P. (2015). Kuramoto model simulation of neural hubs and dynamic synchrony in the human cerebral connectome. *BMC Neuroscience*, 16(1), 16. 10.1186/s12868-015-0193-z
- Schmutz, V., Gerstner, W., & Schwalger, T. (2020). Mesoscopic population equations for spiking neural networks with synaptic short-term plasticity. *Journal of Mathematical Neuroscience*, 10(1), 10. 10.1186/s13408-020-00082-z
- Seliger, P., Young, S. C., & Tsimring, L. S. (2002). Plasticity and learning in a network of coupled phase oscillators. *Physical Review E—Statistical Physics, Plasmas, Fluids, and Related Interdisciplinary Topics*, 65(4), 7. 10.1103/PhysRevE.65.041906
- Sgritta, M., Locatelli, F., Soda, T., Prestori, F., & D'Angelo, E. U. (2017). Hebbian spike-timing dependent plasticity at the cerebellar input stage. *Journal of Neuroscience*, 37(11), 2809–2823. 10.1523/JNEUROSCI.2079-16.2016, PubMed: 28188217
- Snyder, J., Zlotnik, A., & Lokhov, A. Y. (2020). Data-driven selection of coarse-grained models of coupled oscillators. *Physical Review Research*, 2(4), 2. 10.1103/PhysRevResearch.2.043402
- Song, S., Miller, K. D., & Abbott, L. F. (2000). Competitive Hebbian learning through spike-timing-dependent synaptic plasticity. *Nature Neuroscience* 3(9), 919–926. 10.1038/78829, PubMed: 10966623
- Taher, H., Torcini, A., & Olmi, S. (2020). Exact neural mass model for synaptic-based working memory. *PLOS Computational Biology*, 16(12), e1008533. 10.1371/journal.pcbi.1008533
- Tass, P. A., & Majtanik, M. (2006). Long-term anti-kindling effects of desynchronizing brain stimulation: A theoretical study. *Biological Cybernetics*, 94(1), 58–66. 10.1007/s00422-005-0028-6, PubMed: 16284784
- Tass, P. A., Qin, L., Hauptmann, C., Dovero, S., Bezard, E., Boraud, T., & Meissner, W. G. (2012). Coordinated reset has sustained aftereffects in Parkinsonian monkeys. *Annals of Neurology*, 7(5), 816–820. 10.1002/ana.23663
- Thiele, M., Berner, R., Tass, P. A., Schöll, E., & Yanchuk, S. (2023). Asymmetric adaptivity induces recurrent synchronization in complex networks. *Chaos*, 33(2), 33. 10.1063/5.0128102
- Thiem, T. N., Kooshkbaghi, M., Bertalan, T., Laing, C. R., & Kevrekidis, I. G. (2020). Emergent spaces for coupled oscillators. *Frontiers in Computational Neuroscience*, 14, 36. 10.3389/fncom.2020.00036
- Tsodyks, M., Pawelzik, K., & Markram, H. (1998). Neural networks with dynamic synapses. *Neural Computation*, 10(4), 821–835. 10.1162/089976698300017502, PubMed: 9573407
- Tyulkina, I. V., Goldobin, D. S., Klimenko, L. S., & Pikovsky, A. (2018). Dynamics of noisy oscillator populations beyond the Ott-Antonsen ansatz. *Physical Review Letters*, 120(26). 10.1103/PhysRevLett.120.264101

- Vlasov, V., Rosenblum, M., & Pikovsky, A. (2016). Dynamics of weakly inhomogeneous oscillator populations: Perturbation theory on top of Watanabe-Strogatz integrability. *Journal of Physics A: Mathematical and Theoretical*, 49(31), 49LT02. 10.1088/1751-8113/49/31/31LT02
- Wang, J., Nebeck, S., Muralidharan, A., Johnson, M. D., Vitek, J. L., & Baker, K. B. (2016). Coordinated reset deep brain stimulation of subthalamic nucleus produces long-lasting, dose-dependent motor improvements in the 1-methyl-4-phenyl-1,2,3,6-tetrahydropyridine non-human primate model of Parkinsonism. *Brain Stimulation*, 9(4), 609–617. 10.1016/j.brs.2016.03.014, PubMed: 27151601
- Weerasinghe, G., Duchet, B., Bick, C., & Bogacz, R. (2021). Optimal closed-loop deep brain stimulation using multiple independently controlled contacts. *PLOS Computational Biology*, 17(8), e1009281. 10.1371/journal.pcbi.1009281
- Weerasinghe, G., Duchet, B., Cagnan, H., Brown, P., Bick, C., & Bogacz, R. (2019). Predicting the effects of deep brain stimulation using a reduced coupled oscillator model. *PLOS Computational Biology*, 15(8), e1006575. 10.1371/journal.pcbi.1006575
- Wiratman, W., Murakami, T., Tiksnadi, A., Kobayashi, S., Hanajima, R., & Ugawa, Y. (2022). Enhancement of LTD-like plasticity by associative pairing of quadripulse magnetic stimulation with peripheral nerve stimulation. *Clinical Neurophysiology*, 138, 9–17. 10.1016/j.clinph.2022.03.009, PubMed: 35358770

---

Received July 17, 2022; accepted April 26, 2023.